Acta Geophysica (2020) 68:1387–1409
https://doi.org/10.1007/s11600-020-00481-6

RESEARCH ARTICLE - APPLIED GEOPHYSICS

Frequency-domain elastic-wave modeling for polygonal topography using rotated average-derivative difference operators

Zheng Li[1,2,3] · Jing-Bo Chen[1,2,3] · Jian Cao[1,2]

Received: 4 February 2020 / Accepted: 5 September 2020 / Published online: 18 September 2020

Abstract

Modeling of seismic wave propagation in areas with irregular topography is an important topic in the field of seismic exploration. As a popular numerical method for seismic modeling, the finite difference method is nontrivial to consider the irregular free surface. There have been extensive studies on the time-domain finite difference simulations with irregular topography; however, the frequency-domain finite difference simulation considering irregular topography is relatively less studied. The average-derivative approach is an optimal numerical simulation scheme in the frequency domain, which can produce accurate modeling results at a relatively low computational cost. Nevertheless, this approach can only deal with the modeling problems with a flat free surface. To address this issue, we design a new frequency-domain finite difference scheme by introducing the polygonal representation of topography into the average-derivative method. The irregular topography is represented by line segments with various slopes. An extension of the conventional average-derivative difference operator in the local rotated coordinate system is used for formulating the spatial derivatives aligned with the topographic line segments. As a result, new average-derivative difference schemes are obtained for irregular topography. In this way, the average-derivative optimal method is generalized to the model with irregular topography. Numerical examples show the effectiveness of the presented method.

Keywords Irregular topography · Frequency-domain modeling · Rotated coordinate system · Average-derivative difference scheme

Introduction

The surface of the earth is not a flat plane. The irregular surface could distort the recorded data significantly. It also brings new challenge to seismic exploration. Numerical simulations with the surface topography describe more realistic seismic wave propagation. Thus, it is critically useful to study a numerical simulation method that considers the irregular topography.

To incorporate the irregular topography, the numerical methods based on the weak form of wave equation are commonly used. For example, Komatitsch and Tromp (1999) presented seismic wave field simulation with a relief surface by utilizing spectral element method. They discussed disturbance caused by the irregular topography. Finite element method and finite volume method are mostly used in the frequency domain to study seismic wave propagation with irregular topography (Jang et al. 2008; Brossier et al. 2008). Another important approach is to use the strong form of wave equation, such as the finite difference method. Compared with the finite difference method, the finite element method requires high-quality unstructured mesh, which is difficult for a complicated near surface. Moreover, the finite difference method is relatively cheaper in the aspect of computational cost compared to the finite element method.

✉ Zheng Li
lizheng16@mail.iggcas.ac.cn

Jing-Bo Chen
chenjb@mail.iggcas.ac.cn

Jian Cao
caojian@mail.iggcas.ac.cn

[1] Key Laboratory of Petroleum Resources Research, Institute of Geology and Geophysics, Chinese Academy of Sciences, Beijing 100029, China

[2] Innovation Academy for Earth Science, Chinese Academy of Sciences, Beijing 100029, China

[3] University of Chinese Academy of Sciences, Beijing 100049, China

Most of the methods for finite difference modeling with irregular topography are developed in the time domain, while an implementation in the frequency domain is relatively rare. To implement the irregular topography in the frequency domain, an accurate and stable numerical scheme for the frequency-domain elastic-wave equation discretization is necessary. Chen and Cao (2016) developed an average-derivative optimal method for modeling frequency-domain 2D elastic-wave equation. This method has the advantages of memory saving and arbitrary directional sampling intervals, which can reduce the computational cost of the frequency-domain elastic-wave modeling. However, only the flat free surface is considered in Chen and Cao (2016). The effects of the irregular topography are not considered. We generalize the frequency-domain average-derivative optimal method to the irregular topography case in this study.

Within the framework of the finite difference method, several kinds of ways to represent the irregular topography have been developed. A straightforward way is to take advantage of segments with different slopes to fit various topographies. Ilan (1977) applied this approach to match topography and studied propagation features caused by the irregular free surface. Jih et al. (1988) improved the method by taking transition points between different slope segments into account. The whole numerical treatment to the irregular surface is divided into six kinds of cases. In each case, they applied center difference approximation (Alterman and Karal 1968) or one-side difference approximation (Alterman and Rotenberg 1969) as the boundary condition, and they used the standard second-order difference scheme for the internal points (Kelly et al. 1976). We adopt this method in our paper. Another way is to realize topography mapping by coordinate transformation (Tessmer et al. 1992; Hestholm and Ruud 1994, 1998, 2002; Tessmer and Kosloff 1994; Ruud and Hestholm 2001; Lan and Zhang 2011; Zhang et al. 2012; Wang et al. 2015). This method projects a rectangle grid onto a curved grid and implements numerical calculations for free surface on the curved grid. To avoid intricate coordinate transformation, some researchers proposed to use the staircase approximation (Robertsson 1996; Ohminato and Chouet 1997; Hayashi et al. 2001). The irregular surface is represented by rectangle grids directly in this method. The implementation for the irregular free-surface boundary condition is an extension of the treatment for horizontal free surface. This method is suitable for arbitrary topography. However, the scattered noise occurs because of staircase-shaped discretization, which can be eliminated by an oversampled grid.

In our paper, we design a new frequency-domain finite difference scheme to implement the polygonal topography. This method is a generalization of the conventional average-derivative method proposed with a flat free surface (Chen and Cao 2016). We use a local rotated coordinate method to generalize the conventional average-derivative difference operators into the rotated coordinate system aligned with the irregular free surface. The local rotated coordinate method is presented by Jih et al. (1988) in the time domain. We classify the implementation of the irregular free surface into nine cases. New average-derivative schemes are presented for the irregular topography. These new schemes generalize the conventional average-derivative method to models with irregular topography easily.

In the following section, we present the theory of our method. This is followed by derivation of the new numerical schemes at the irregular free surface. We analyze the effectiveness through a simple model test. The influences on the structure of impedance matrix are also examined. Finally, we provide some complex numerical examples to demonstrate the feasibility of our new method.

Theory

Modeling with irregular free surface

We consider the first-order elastic-wave equation in frequency domain

$$\begin{cases} \rho\omega^2 u + \frac{\partial \tau_{xx}}{\partial x} + \frac{\partial \tau_{xz}}{\partial z} = 0, \\ \rho\omega^2 w + \frac{\partial \tau_{zx}}{\partial x} + \frac{\partial \tau_{zz}}{\partial z} = 0, \\ \tau_{xx} = (\lambda + 2\mu)\frac{\partial u}{\partial x} + \lambda\frac{\partial w}{\partial z}, \\ \tau_{zz} = (\lambda + 2\mu)\frac{\partial w}{\partial z} + \lambda\frac{\partial u}{\partial x}, \\ \tau_{xz} = \tau_{zx} = \mu\left(\frac{\partial u}{\partial z} + \frac{\partial w}{\partial x}\right), \end{cases} \tag{1}$$

where ρ is the density, ω denotes the angular frequency, λ and μ are Lamé parameters, u and w represent components of displacements in horizontal and vertical directions, respectively, τ_{xx} and τ_{zz} are normal stress components, and τ_{xz} and τ_{zx} are shear stress components.

Eliminating the stress components in the first two equations by inserting the last three expressions of Eq. (1) into the first two equations, we obtain the elastic-wave equation in terms of displacements

$$\begin{cases} \rho\omega^2 u + \frac{\partial}{\partial x}\left(\eta\frac{\partial u}{\partial x}\right) + \frac{\partial}{\partial z}\left(\mu\frac{\partial u}{\partial z}\right) + \frac{\partial}{\partial x}\left(\lambda\frac{\partial w}{\partial z}\right) + \frac{\partial}{\partial z}\left(\mu\frac{\partial w}{\partial x}\right) = 0, \\ \rho\omega^2 w + \frac{\partial}{\partial x}\left(\mu\frac{\partial w}{\partial x}\right) + \frac{\partial}{\partial z}\left(\eta\frac{\partial w}{\partial z}\right) + \frac{\partial}{\partial x}\left(\mu\frac{\partial u}{\partial z}\right) + \frac{\partial}{\partial z}\left(\lambda\frac{\partial u}{\partial x}\right) = 0. \end{cases} \tag{2}$$

Here, we replace $\lambda + 2\mu$ by η.

To perform seismic numerical modeling in the presence of topography, we deal with the internal model and the irregular free surface, respectively. For the internal model, we use the conventional average-derivative method to discretize Eq. (2) and obtain a 9-point scheme (Chen and Cao 2016).

Except for the free surface, the remaining three boundaries are handled with perfectly matched layer (PML) boundary conditions. To fill into the "finite-difference star" proposed by Pratt (1990), the 9-point scheme in Chen and Cao (2016) was simplified into

$$\begin{cases} c_1 u_{r-1,s-1} + c_2 u_{r,s-1} + c_3 u_{r+1,s-1} + c_4 u_{r-1,s} + c_5 u_{r,s} + c_6 u_{r+1,s} + c_7 u_{r-1,s+1} + c_8 u_{r,s+1} \\ +c_9 u_{r+1,s+1} + d_1 w_{r-1,s-1} + d_2 w_{r+1,s-1} + d_3 w_{r-1,s+1} + d_4 w_{r+1,s+1} = 0, \\ \tilde{d}_1 w_{r-1,s-1} + \tilde{d}_2 w_{r,s-1} + \tilde{d}_3 w_{r+1,s-1} + \tilde{d}_4 w_{r-1,s} + \tilde{d}_5 w_{r,s} + \tilde{d}_6 w_{r+1,s} + \tilde{d}_7 w_{r-1,s+1} + \tilde{d}_8 w_{r,s+1} \\ +\tilde{d}_9 w_{r+1,s+1} + \tilde{c}_1 u_{r-1,s-1} + \tilde{c}_2 u_{r+1,s-1} + \tilde{c}_3 u_{r-1,s+1} + \tilde{c}_4 u_{r+1,s+1} = 0. \end{cases} \tag{3}$$

The expressions for $c_i, \tilde{d}_i (i = 1, 2, \ldots, 9)$ and $d_j, \tilde{c}_j (j = 1, 2, 3, 4)$ can be found in Chen and Cao (2016).

To obtain new numerical schemes at the irregular free surface, we use the local rotated coordinate method presented by Jih et al. (1988). We develop this approach in the frequency domain (see "Appendix 1"). For the convenience of subsequent derivations of the new numerical scheme on the free surface, we summarize numerical treatments to the irregular free surface which are carried out by Jih et al. (1988) in time domain. In order to expound the main idea of our theory clearly, we use a free surface with a 45° slope (Fig. 1). The new scheme derived at this simple polygonal-shaped free surface can be generalized to more complex irregular topographies easily.

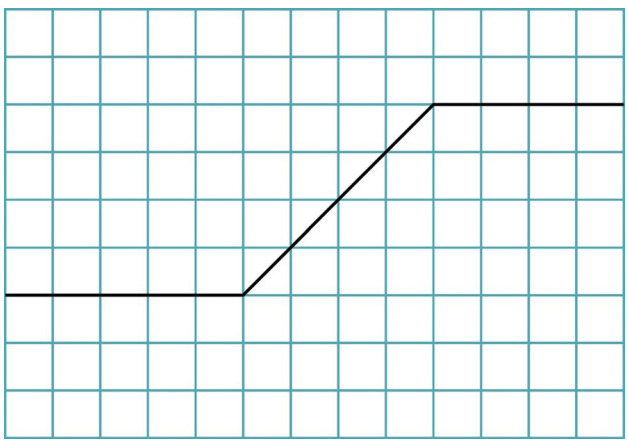

Fig. 1 Structure of the irregular free surface

The key point of our method is designing new average-derivative difference schemes aligned with the irregular free surface by a local rotated coordinate method. Using our new numerical schemes, the elastic-wave modeling for irregular topography can be implemented in the frequency domain.

The numerical schemes on the slope surface are derived by a combination of the average-derivative method and the local rotated coordinate method. These numerical schemes differ in the number and distribution of the discrete grid points involved. Therefore, the guideline on determining different cases is the number and distribution of the discrete grid points involved. By checking all the points along the slope surface, we have found 9 cases in which the number and distribution of the discrete grid points involved differ from each other.

Here, we derive the new numerical schemes in these nine cases, respectively.

(1) Case 1

According to Fig. 2, the first case contains points on the left of point 1 and the right of point 2 on the free surface.

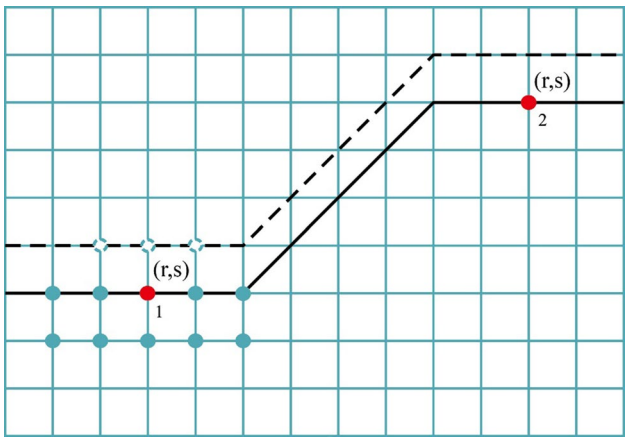

Fig. 2 Simulation points and discrete grid points used for the first case. Here, red points are the simulation points, blue points are discrete grid points used by the new average-derivative scheme, and points with dashed line on the fiction line are discrete grid points used by the conventional average-derivative scheme

Point 1 and point 2 are also involved. Based on the conventional average-derivative approach, nine points should be used to discrete the elastic-wave equation. However, three of them are outside the model according to Fig. 2. The numerical expressions for these three points are introduced in "Appendix 1." The average-derivative difference operators are changed. The new average-derivative difference scheme on the irregular free surface for this case can be derived. To fit the "star" proposed by Pratt (1990), we can simplify the new numerical scheme into the following expressions:

$$\begin{cases} c_{11}u_{r-2,s} + c_{12}u_{r-2,s+1} + c_{13}u_{r-1,s} + c_{14}u_{r-1,s+1} + c_{15}u_{r,s} \\ +c_{16}u_{r,s+1} + c_{17}u_{r+1,s} + c_{18}u_{r+1,s+1} + c_{19}u_{r+2,s} + c_{110}u_{r+2,s+1} \\ +d_{11}w_{r-2,s} + d_{12}w_{r-2,s+1} + d_{13}w_{r-1,s} + d_{14}w_{r-1,s+1} + d_{15}w_{r,s} \\ +d_{16}w_{r,s+1} + d_{17}w_{r+1,s} + d_{18}w_{r+1,s+1} + d_{19}w_{r+2,s} + d_{110}w_{r+2,s+1} = 0, \\ \tilde{d}_{11}w_{r-2,s} + \tilde{d}_{12}w_{r-2,s+1} + \tilde{d}_{13}w_{r-1,s} + \tilde{d}_{14}w_{r-1,s+1} + \tilde{d}_{15}w_{r,s} \\ +\tilde{d}_{16}w_{r,s+1} + \tilde{d}_{17}w_{r+1,s} + \tilde{d}_{18}w_{r+1,s+1} + \tilde{d}_{19}w_{r+2,s} + \tilde{d}_{110}w_{r+2,s+1} \\ +\tilde{c}_{11}u_{r-2,s} + \tilde{c}_{12}u_{r-2,s+1} + \tilde{c}_{13}u_{r-1,s} + \tilde{c}_{14}u_{r-1,s+1} + \tilde{c}_{15}u_{r,s} \\ +\tilde{c}_{16}u_{r,s+1} + \tilde{c}_{17}u_{r+1,s} + \tilde{c}_{18}u_{r+1,s+1} + \tilde{c}_{19}u_{r+2,s} + \tilde{c}_{110}u_{r+2,s+1} = 0, \end{cases} \tag{4}$$

where $c_{ij}, \tilde{d}_{ij}$ and $d_{ij}, \tilde{c}_{ij} (i = 1, j = 1, 2, \ldots, 10)$ are the coefficients.

Discrete grid points used by our new numerical scheme are shown in Fig. 2, which are blue and red points. In order to describe the difference between the new and the conventional average-derivative difference scheme, we simplify the coefficients of the new difference scheme. Here, we observe that new coefficients consist of the coefficients $c_i, \tilde{d}_i (i = 1, 2, \ldots, 9)$ and $d_j, \tilde{c}_j (j = 1, 2, 3, 4)$ of the conventional average-derivative difference scheme. Expressions for new coefficients are

$$\begin{aligned} c_{11} &= -d_1 \frac{1}{S_{xr-1}} \frac{\lambda_{r-1,s}}{\eta_{r-1,s}} \frac{\Delta z}{2\Delta x}, \\ c_{12} &= 0, \\ c_{13} &= c_1 + c_4, \\ c_{14} &= c_7, \\ c_{15} &= c_2 + c_5 + d_1 \frac{1}{S_{xr-1}} \frac{\lambda_{r-1,s}}{\eta_{r-1,s}} \frac{\Delta z}{2\Delta x} - d_2 \frac{1}{S_{xr+1}} \frac{\lambda_{r+1,s}}{\eta_{r+1,s}} \frac{\Delta z}{2\Delta x}, \\ c_{16} &= c_8, \\ c_{17} &= c_3 + c_6, \\ c_{18} &= c_9, \\ c_{19} &= d_2 \frac{1}{S_{xr+1}} \frac{\lambda_{r+1,s}}{\eta_{r+1,s}} \frac{\Delta z}{2\Delta x}, \\ c_{110} &= 0, \end{aligned} \tag{5}$$

$$\begin{aligned} d_{11} &= -c_1 \frac{1}{S_{xr-1}} \frac{\Delta z}{2\Delta x}, \\ d_{12} &= 0, \\ d_{13} &= -c_2 \frac{1}{S_{xr}} \frac{\Delta z}{2\Delta x} + d_1, \\ d_{14} &= d_3, \\ d_{15} &= c_1 \frac{1}{S_{xr-1}} \frac{\Delta z}{2\Delta x} - c_3 \frac{1}{S_{xr+1}} \frac{\Delta z}{2\Delta x}, \\ d_{16} &= 0, \\ d_{17} &= c_2 \frac{1}{S_{xr}} \frac{\Delta z}{2\Delta x} + d_2, \\ d_{18} &= d_4, \\ d_{19} &= c_3 \frac{1}{S_{xr+1}} \frac{\Delta z}{2\Delta x}, \\ d_{110} &= 0, \end{aligned} \tag{6}$$

and

$$\begin{aligned} \tilde{c}_{11} &= -\tilde{d}_1 \frac{1}{S_{xr-1}} \frac{\lambda_{r-1,s}}{\eta_{r-1,s}} \frac{\Delta z}{2\Delta x}, \\ \tilde{c}_{12} &= 0, \\ \tilde{c}_{13} &= -\tilde{d}_2 \frac{1}{S_{xr}} \frac{\lambda_{r,s}}{\eta_{r,s}} \frac{\Delta z}{2\Delta x} + \tilde{c}_1, \\ \tilde{c}_{14} &= \tilde{c}_3, \\ \tilde{c}_{15} &= \tilde{d}_1 \frac{1}{S_{xr-1}} \frac{\lambda_{r-1,s}}{\eta_{r-1,s}} \frac{\Delta z}{2\Delta x} - \tilde{d}_3 \frac{1}{S_{xr+1}} \frac{\lambda_{r+1,s}}{\eta_{r+1,s}} \frac{\Delta z}{2\Delta x}, \\ \tilde{c}_{16} &= 0, \\ \tilde{c}_{17} &= \tilde{d}_2 \frac{1}{S_{xr}} \frac{\lambda_{r,s}}{\eta_{r,s}} \frac{\Delta z}{2\Delta x} + \tilde{c}_2, \\ \tilde{c}_{18} &= \tilde{c}_4, \\ \tilde{c}_{19} &= \tilde{d}_3 \frac{1}{S_{xr+1}} \frac{\lambda_{r+1,s}}{\eta_{r+1,s}} \frac{\Delta z}{2\Delta x}, \\ \tilde{c}_{110} &= 0, \end{aligned} \tag{7}$$

$$
\begin{aligned}
\tilde{d}_{11} &= -\tilde{c}_1 \frac{1}{S_{xr-1}} \frac{\Delta z}{2\Delta x},\\
\tilde{d}_{12} &= 0,\\
\tilde{d}_{13} &= \tilde{d}_1 + \tilde{d}_4,\\
\tilde{d}_{14} &= \tilde{d}_7,\\
\tilde{d}_{15} &= \tilde{d}_2 + \tilde{d}_5 + \tilde{c}_1 \frac{1}{S_{xr-1}} \frac{\Delta z}{2\Delta x} - \tilde{c}_2 \frac{1}{S_{xr+1}} \frac{\Delta z}{2\Delta x},\\
\tilde{d}_{16} &= \tilde{d}_8,\\
\tilde{d}_{17} &= \tilde{d}_3 + \tilde{d}_6,\\
\tilde{d}_{18} &= \tilde{d}_9,\\
\tilde{d}_{19} &= \tilde{c}_2 \frac{1}{S_{xr+1}} \frac{\Delta z}{2\Delta x},\\
\tilde{d}_{110} &= 0,
\end{aligned}
\tag{8}
$$

where Δx and Δz denote spacing intervals.

Here, we have

$$
\begin{cases}
S_x = 1 - \frac{ic_x}{\omega} \cos\left(\frac{\pi}{2}\frac{x}{L_x}\right),\\
S_z = 1 - \frac{ic_z}{\omega} \cos\left(\frac{\pi}{2}\frac{z}{L_z}\right),
\end{cases}
\tag{9}
$$

where c_x and c_z are the coefficients in Operto et al. (2007); L_x and L_z are thickness along x- and z-direction. On the free surface, we have $S_z = 1$.

(2) Case 2

The simulation point in the second case is on the left of the flat-to-slope transition point (Fig. 3). According to the 9-point scheme, three points are on the fiction line. The numerical expressions at these points are given in "Appendix 1." The average-derivative difference operators are changed. We derive the new average-derivative scheme. Discrete grid points used by our scheme are shown in Fig. 3. They are denoted by blue and red points. We can rewrite the new numerical scheme as follows:

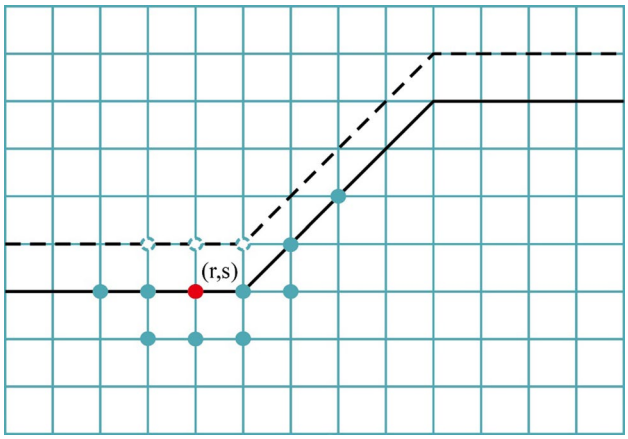

Fig. 3 Simulation point and discrete grid points used for the second case

$$
\begin{aligned}
c_{21} &= -d_1 \frac{\lambda_{r-1,s}}{\eta_{r-1,s}} \frac{\Delta z}{2\Delta x},\\
c_{22} &= c_1 + c_3 \frac{1}{2}(1-\varepsilon_1) \frac{\lambda_{r,s}}{\eta_{r,s}} \frac{\Delta z}{2\Delta x} + c_4,\\
c_{23} &= c_7,\\
c_{24} &= c_2 + c_5 + d_1 \frac{\lambda_{r-1,s}}{\eta_{r-1,s}} \frac{\Delta z}{2\Delta x} - d_2 \frac{1}{2} \frac{\lambda_{r+1,s-1}}{\eta_{r+1,s-1}},\\
c_{25} &= c_8,\\
c_{26} &= c_3 \left[(1-\varepsilon_0) - \frac{1}{2}(1-\varepsilon_1) \frac{\lambda_{r,s}}{\eta_{r,s}} \frac{\Delta z}{2\Delta x}\right] + c_6,\\
c_{27} &= c_9,\\
c_{28} &= -c_3 \frac{1}{2} \varepsilon_1 \frac{1}{2} \frac{\lambda_{r+2,s-2}}{\eta_{r+2,s-2}} + d_2 \frac{1}{2} \frac{\lambda_{r+1,s-1}}{\eta_{r+1,s-1}} \left(1 - \varepsilon_1 \varepsilon_0'\right),\\
c_{29} &= c_3 \varepsilon_0,\\
c_{210} &= c_3 \frac{1}{2} \varepsilon_1 \frac{1}{2} \frac{\lambda_{r+2,s-2}}{\eta_{r+2,s-2}} + d_2 \frac{1}{2} \frac{\lambda_{r+1,s-1}}{\eta_{r+1,s-1}} \varepsilon_1 \varepsilon_0',
\end{aligned}
\tag{11}
$$

$$
\begin{cases}
c_{21}u_{r-2,s} + c_{22}u_{r-1,s} + c_{23}u_{r-1,s+1} + c_{24}u_{r,s} + c_{25}u_{r,s+1}\\
+c_{26}u_{r+1,s} + c_{27}u_{r+1,s+1} + c_{28}u_{r+2,s-1} + c_{29}u_{r+2,s} + c_{210}u_{r+3,s-2}\\
+d_{21}w_{r-2,s} + d_{22}w_{r-1,s} + d_{23}w_{r-1,s+1} + d_{24}w_{r,s} + d_{25}w_{r,s+1}\\
+d_{26}w_{r+1,s} + d_{27}w_{r+1,s+1} + d_{28}w_{r+2,s-1} + d_{29}w_{r+2,s} + d_{210}w_{r+3,s-2} = 0,\\
\tilde{d}_{21}w_{r-2,s} + \tilde{d}_{22}w_{r-1,s} + \tilde{d}_{23}w_{r-1,s+1} + \tilde{d}_{24}w_{r,s} + \tilde{d}_{25}w_{r,s+1}\\
+\tilde{d}_{26}w_{r+1,s} + \tilde{d}_{27}w_{r+1,s+1} + \tilde{d}_{28}w_{r+2,s-1} + \tilde{d}_{29}w_{r+2,s} + \tilde{d}_{210}w_{r+3,s-2}\\
+\tilde{c}_{21}u_{r-2,s} + \tilde{c}_{22}u_{r-1,s} + \tilde{c}_{23}u_{r-1,s+1} + \tilde{c}_{24}u_{r,s} + \tilde{c}_{25}u_{r,s+1}\\
+\tilde{c}_{26}u_{r+1,s} + \tilde{c}_{27}u_{r+1,s+1} + \tilde{c}_{28}u_{r+2,s-1} + \tilde{c}_{29}u_{r+2,s} + \tilde{c}_{210}u_{r+3,s-2} = 0,
\end{cases}
\tag{10}
$$

where

$$
\begin{aligned}
d_{21} &= -c_1\frac{\Delta z}{2\Delta x},\\
d_{22} &= -c_2\frac{\Delta z}{2\Delta x} + d_1 + d_2\frac{1}{2}\frac{\lambda_{r+1,s-1}}{\eta_{r+1,s-1}}(1-\varepsilon_1)\frac{\Delta z}{2\Delta x},\\
d_{23} &= d_3,\\
d_{24} &= c_1\frac{\Delta z}{2\Delta x} - c_3\frac{1}{2},\\
d_{25} &= 0,\\
d_{26} &= c_2\frac{\Delta z}{2\Delta x} + d_2\left[(1-\varepsilon_0) - \frac{1}{2}\frac{\lambda_{r+1,s-1}}{\eta_{r+1,s-1}}(1-\varepsilon_1)\frac{\Delta z}{2\Delta x}\right],\\
d_{27} &= d_4,\\
d_{28} &= c_3\frac{1}{2}\left(1-\varepsilon_1\varepsilon_0'\right) - d_2\frac{1}{2}\frac{\lambda_{r+1,s-1}}{\eta_{r+1,s-1}}\varepsilon_1\frac{1}{2},\\
d_{29} &= d_2\varepsilon_0,\\
d_{210} &= c_3\frac{1}{2}\varepsilon_1\varepsilon_0' + d_2\frac{1}{2}\frac{\lambda_{r+1,s-1}}{\eta_{r+1,s-1}}\varepsilon_1\frac{1}{2},
\end{aligned}
\tag{12}
$$

and

$$
\begin{aligned}
\tilde{c}_{21} &= -\tilde{d}_1\frac{\lambda_{r-1,s}}{\eta_{r-1,s}}\frac{\Delta z}{2\Delta x},\\
\tilde{c}_{22} &= -\tilde{d}_2\frac{\lambda_{r,s}}{\eta_{r,s}}\frac{\Delta z}{2\Delta x} + \tilde{c}_1 + \tilde{c}_2\frac{1}{2}(1-\varepsilon_1)\frac{\lambda_{r,s}}{\eta_{r,s}}\frac{\Delta z}{2\Delta x},\\
\tilde{c}_{23} &= \tilde{c}_3,\\
\tilde{c}_{24} &= \tilde{d}_1\frac{\lambda_{r-1,s}}{\eta_{r-1,s}}\frac{\Delta z}{2\Delta x} - \tilde{d}_3\frac{1}{2}\frac{\lambda_{r+1,s-1}}{\eta_{r+1,s-1}},\\
\tilde{c}_{25} &= 0,\\
\tilde{c}_{26} &= \tilde{d}_2\frac{\lambda_{r,s}}{\eta_{r,s}}\frac{\Delta z}{2\Delta x} + \tilde{c}_2\left[(1-\varepsilon_0) - \frac{1}{2}(1-\varepsilon_1)\frac{\lambda_{r,s}}{\eta_{r,s}}\frac{\Delta z}{2\Delta x}\right],\\
\tilde{c}_{27} &= \tilde{c}_4,\\
\tilde{c}_{28} &= \tilde{d}_3\frac{1}{2}\frac{\lambda_{r+1,s-1}}{\eta_{r+1,s-1}}\left(1-\varepsilon_1\varepsilon_0'\right) - \tilde{c}_2\frac{1}{2}\varepsilon_1\frac{1}{2}\frac{\lambda_{r+2,s-2}}{\eta_{r+2,s-2}},\\
\tilde{c}_{29} &= \tilde{c}_2\varepsilon_0,\\
\tilde{c}_{210} &= \tilde{d}_3\frac{1}{2}\frac{\lambda_{r+1,s-1}}{\eta_{r+1,s-1}}\varepsilon_1\varepsilon_0' + \tilde{c}_2\frac{1}{2}\varepsilon_1\frac{1}{2}\frac{\lambda_{r+2,s-2}}{\eta_{r+2,s-2}},
\end{aligned}
\tag{13}
$$

$$
\begin{aligned}
\tilde{d}_{21} &= -\tilde{c}_1\frac{\Delta z}{2\Delta x},\\
\tilde{d}_{22} &= \tilde{d}_1 + \tilde{d}_3\frac{1}{2}\frac{\lambda_{r+1,s-1}}{\eta_{r+1,s-1}}(1-\varepsilon_1)\frac{\Delta z}{2\Delta x} + \tilde{d}_4,\\
\tilde{d}_{23} &= \tilde{d}_7,\\
\tilde{d}_{24} &= \tilde{d}_2 + \tilde{d}_5 + \tilde{c}_1\frac{\Delta z}{2\Delta x} - \tilde{c}_2\frac{1}{2},\\
\tilde{d}_{25} &= \tilde{d}_8,\\
\tilde{d}_{26} &= \tilde{d}_3\left[(1-\varepsilon_0) - \frac{1}{2}\frac{\lambda_{r+1,s-1}}{\eta_{r+1,s-1}}(1-\varepsilon_1)\frac{\Delta z}{2\Delta x}\right] + \tilde{d}_6,\\
\tilde{d}_{27} &= \tilde{d}_9,\\
\tilde{d}_{28} &= -\tilde{d}_3\frac{1}{2}\frac{\lambda_{r+1,s-1}}{\eta_{r+1,s-1}}\varepsilon_1\frac{1}{2} + \tilde{c}_2\frac{1}{2}\left(1-\varepsilon_1\varepsilon_0'\right),\\
\tilde{d}_{29} &= \tilde{d}_3\varepsilon_0,\\
\tilde{d}_{210} &= \tilde{d}_3\frac{1}{2}\frac{\lambda_{r+1,s-1}}{\eta_{r+1,s-1}}\varepsilon_1\frac{1}{2} + \tilde{c}_2\frac{1}{2}\varepsilon_1\varepsilon_0'.
\end{aligned}
\tag{14}
$$

(3) Case 3

The simulation point in the third case is the red point in Fig. 4. It is on the right of the slope-to-flat transition point.

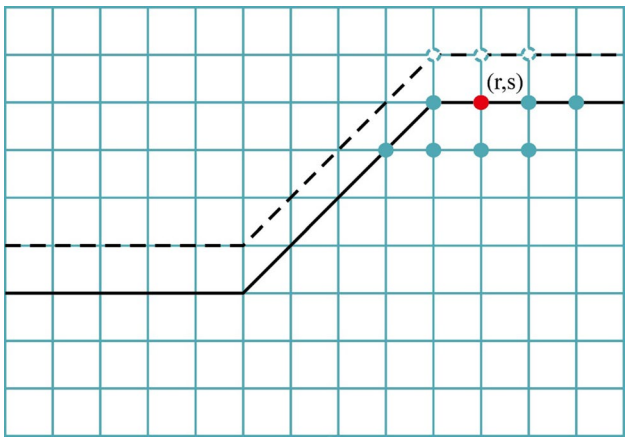

Fig. 4 Simulation point and discrete grid points used for the third case

Three discrete grid points are located on the fiction line when using the conventional average-derivative scheme. We derive the new average-derivative scheme using the numerical expressions at these three points given in "Appendix 1." Discrete grid points used by our scheme are shown in Fig. 4 (blue and red points). The new numerical scheme for this case can be simplified as follows:

$$\begin{cases} c_{31}u_{r-2,s+1}+c_{32}u_{r-1,s}+c_{33}u_{r-1,s+1}+c_{34}u_{r,s} \\ +c_{35}u_{r,s+1}+c_{36}u_{r+1,s}+c_{37}u_{r+1,s+1}+c_{38}u_{r+2,s} \\ +d_{31}w_{r-2,s+1}+d_{32}w_{r-1,s}+d_{33}w_{r-1,s+1}+d_{34}w_{r,s} \\ +d_{35}w_{r,s+1}+d_{36}w_{r+1,s}+d_{37}w_{r+1,s+1}+d_{38}w_{r+2,s}=0, \\ \tilde{d}_{31}w_{r-2,s+1}+\tilde{d}_{32}w_{r-1,s}+\tilde{d}_{33}w_{r-1,s+1}+\tilde{d}_{34}w_{r,s} \\ +\tilde{d}_{35}w_{r,s+1}+\tilde{d}_{36}w_{r+1,s}+\tilde{d}_{37}w_{r+1,s+1}+\tilde{d}_{38}w_{r+2,s} \\ +\tilde{c}_{31}u_{r-2,s+1}+\tilde{c}_{32}u_{r-1,s}+\tilde{c}_{33}u_{r-1,s+1}+\tilde{c}_{34}u_{r,s} \\ +\tilde{c}_{35}u_{r,s+1}+\tilde{c}_{36}u_{r+1,s}+\tilde{c}_{37}u_{r+1,s+1}+\tilde{c}_{38}u_{r+2,s}=0, \end{cases} \tag{15}$$

where

$$\begin{aligned} c_{31} &= c_1\frac{1}{2}(1-\varepsilon_{11})\frac{1}{2}\frac{\lambda_{r-2,s}}{\eta_{r-2,s}}-d_1\frac{1}{2}\frac{\lambda_{r-1,s-1}}{\eta_{r-1,s-1}}\left[\varepsilon_{11}+(1-\varepsilon_{11})\left(1-\varepsilon_0'\right)\right], \\ c_{32} &= c_1\left[(1-\varepsilon_{00})-\frac{1}{2}\varepsilon_{11}\frac{\lambda_{r,s}}{\eta_{r,s}}\frac{\Delta z}{2\Delta x}-\frac{1}{2}(1-\varepsilon_{11})\frac{1}{2}\frac{\lambda_{r-2,s}}{\eta_{r-2,s}}\right] \\ &\quad +c_4-d_1\frac{1}{2}\frac{\lambda_{r-1,s-1}}{\eta_{r-1,s-1}}(1-\varepsilon_{11})\varepsilon_0', \\ c_{33} &= c_7, \\ c_{34} &= c_1\varepsilon_{00}+c_2+c_5+d_1\frac{1}{2}\frac{\lambda_{r-1,s-1}}{\eta_{r-1,s-1}}-d_2\frac{\lambda_{r+1,s}}{\eta_{r+1,s}}\frac{\Delta z}{2\Delta x}, \\ c_{35} &= c_8, \\ c_{36} &= c_1\frac{1}{2}\varepsilon_{11}\frac{\lambda_{r,s}}{\eta_{r,s}}\frac{\Delta z}{2\Delta x}+c_3+c_6, \\ c_{37} &= c_9, \\ c_{38} &= d_2\frac{\lambda_{r+1,s}}{\eta_{r+1,s}}\frac{\Delta z}{2\Delta x}, \end{aligned} \tag{16}$$

$$\begin{aligned} d_{31} &= -c_1\frac{1}{2}\left[\varepsilon_{11}+(1-\varepsilon_{11})\left(1-\varepsilon_0'\right)\right]+d_1\frac{1}{2}\frac{\lambda_{r-1,s-1}}{\eta_{r-1,s-1}}(1-\varepsilon_{11})\frac{1}{2}, \\ d_{32} &= -c_1\frac{1}{2}(1-\varepsilon_{11})\varepsilon_0'-c_2\frac{\Delta z}{2\Delta x} \\ &\quad +d_1\left[(1-\varepsilon_{00})-\frac{1}{2}\frac{\lambda_{r-1,s-1}}{\eta_{r-1,s-1}}\varepsilon_{11}\frac{\Delta z}{2\Delta x}-\frac{1}{2}\frac{\lambda_{r-1,s-1}}{\eta_{r-1,s-1}}(1-\varepsilon_{11})\frac{1}{2}\right], \\ d_{33} &= d_3, \\ d_{34} &= c_1\frac{1}{2}-c_3\frac{\Delta z}{2\Delta x}+d_1\varepsilon_{00}, \\ d_{35} &= 0, \\ d_{36} &= c_2\frac{\Delta z}{2\Delta x}+d_1\frac{1}{2}\frac{\lambda_{r-1,s-1}}{\eta_{r-1,s-1}}\varepsilon_{11}\frac{\Delta z}{2\Delta x}+d_2, \\ d_{37} &= d_4, \\ d_{38} &= c_3\frac{\Delta z}{2\Delta x}, \end{aligned} \tag{17}$$

and

$$\begin{aligned} \tilde{c}_{31} &= -\tilde{d}_1\frac{1}{2}\frac{\lambda_{r-1,s-1}}{\eta_{r-1,s-1}}[\varepsilon_{11}+(1-\varepsilon_{11})(1-\varepsilon_0')]+\tilde{c}_1\frac{1}{2}(1-\varepsilon_{11})\frac{1}{2}\frac{\lambda_{r-2,s}}{\eta_{r-2,s}}, \\ \tilde{c}_{32} &= -\tilde{d}_1\frac{1}{2}\frac{\lambda_{r-1,s-1}}{\eta_{r-1,s-1}}(1-\varepsilon_{11})\varepsilon_0'-\tilde{d}_2\frac{\lambda_{r,s}}{\eta_{r,s}}\frac{\Delta z}{2\Delta x} \\ &\quad +\tilde{c}_1\left[(1-\varepsilon_{00})-\frac{1}{2}\varepsilon_{11}\frac{\lambda_{r,s}}{\eta_{r,s}}\frac{\Delta z}{2\Delta x}-\frac{1}{2}(1-\varepsilon_{11})\frac{1}{2}\frac{\lambda_{r-2,s}}{\eta_{r-2,s}}\right], \\ \tilde{c}_{33} &= \tilde{c}_3, \\ \tilde{c}_{34} &= \tilde{d}_1\frac{1}{2}\frac{\lambda_{r-1,s-1}}{\eta_{r-1,s-1}}-\tilde{d}_3\frac{\lambda_{r+1,s}}{\eta_{r+1,s}}\frac{\Delta z}{2\Delta x}+\tilde{c}_1\varepsilon_{00}, \\ \tilde{c}_{35} &= 0, \\ \tilde{c}_{36} &= \tilde{d}_2\frac{\lambda_{r,s}}{\eta_{r,s}}\frac{\Delta z}{2\Delta x}+\tilde{c}_1\frac{1}{2}\varepsilon_{11}\frac{\lambda_{r,s}}{\eta_{r,s}}\frac{\Delta z}{2\Delta x}+\tilde{c}_2, \\ \tilde{c}_{37} &= \tilde{c}_4, \\ \tilde{c}_{38} &= \tilde{d}_3\frac{\lambda_{r+1,s}}{\eta_{r+1,s}}\frac{\Delta z}{2\Delta x}, \end{aligned} \tag{18}$$

$$\begin{aligned} \tilde{d}_{31} &= \tilde{d}_1\frac{1}{2}\frac{\lambda_{r-1,s-1}}{\eta_{r-1,s-1}}(1-\varepsilon_{11})\frac{1}{2}-\tilde{c}_1\frac{1}{2}\left[\varepsilon_{11}+(1-\varepsilon_{11})\left(1-\varepsilon_0'\right)\right], \\ \tilde{d}_{32} &= \tilde{d}_1\left[(1-\varepsilon_{00})-\frac{1}{2}\frac{\lambda_{r-1,s-1}}{\eta_{r-1,s-1}}\varepsilon_{11}\frac{\Delta z}{2\Delta x}-\frac{1}{2}\frac{\lambda_{r-1,s-1}}{\eta_{r-1,s-1}}(1-\varepsilon_{11})\frac{1}{2}\right] \\ &\quad +\tilde{d}_4-\tilde{c}_1\frac{1}{2}(1-\varepsilon_{11})\varepsilon_0', \\ \tilde{d}_{33} &= \tilde{d}_7, \\ \tilde{d}_{34} &= \tilde{d}_1\varepsilon_{00}+\tilde{d}_2+\tilde{d}_5+\tilde{c}_1\frac{1}{2}-\tilde{c}_2\frac{\Delta z}{2\Delta x}, \\ \tilde{d}_{35} &= \tilde{d}_8, \\ \tilde{d}_{36} &= \tilde{d}_1\frac{1}{2}\frac{\lambda_{r-1,s-1}}{\eta_{r-1,s-1}}\varepsilon_{11}\frac{\Delta z}{2\Delta x}+\tilde{d}_3+\tilde{d}_6, \\ \tilde{d}_{37} &= \tilde{d}_9, \\ \tilde{d}_{38} &= \tilde{c}_2\frac{\Delta z}{2\Delta x}. \end{aligned} \tag{19}$$

(4) Case 4

The simulation point in the fourth case is the flat-to-slope transition point in Fig. 5. According to the conventional average-derivative approach, there are two discrete grid points outside the model. Based on the numerical expressions at these two points given in "Appendix 1", the new average-derivative scheme is derived. Blue and red points in Fig. 5 are the discrete grid points used by our new scheme. We simplify the new numerical scheme by

$$\begin{cases} c_{41}u_{r-2,s}+c_{42}u_{r-1,s}+c_{43}u_{r-1,s+1}+c_{44}u_{r,s}+c_{45}u_{r,s+1} \\ +c_{46}u_{r+1,s-1}+c_{47}u_{r+1,s}+c_{48}u_{r+1,s+1}+c_{49}u_{r+2,s-2}+d_{41}w_{r-2,s} \\ +d_{42}w_{r-1,s}+d_{43}w_{r-1,s+1}+d_{44}w_{r,s}+d_{45}w_{r,s+1}+d_{46}w_{r+1,s-1} \\ +d_{47}w_{r+1,s}+d_{48}w_{r+1,s+1}+d_{49}w_{r+2,s-2}=0, \\ \tilde{d}_{41}w_{r-2,s}+\tilde{d}_{42}w_{r-1,s}+\tilde{d}_{43}w_{r-1,s+1}+\tilde{d}_{44}w_{r,s}+\tilde{d}_{45}w_{r,s+1} \\ +\tilde{d}_{46}w_{r+1,s-1}+\tilde{d}_{47}w_{r+1,s}+\tilde{d}_{48}w_{r+1,s+1}+\tilde{d}_{49}w_{r+2,s-2}+\tilde{c}_{41}u_{r-2,s} \\ +\tilde{c}_{42}u_{r-1,s}+\tilde{c}_{43}u_{r-1,s+1}+\tilde{c}_{44}u_{r,s}+\tilde{c}_{45}u_{r,s+1}+\tilde{c}_{46}u_{r+1,s-1} \\ +\tilde{c}_{47}u_{r+1,s}+\tilde{c}_{48}u_{r+1,s+1}+\tilde{c}_{49}u_{r+2,s-2}=0, \end{cases} \tag{20}$$

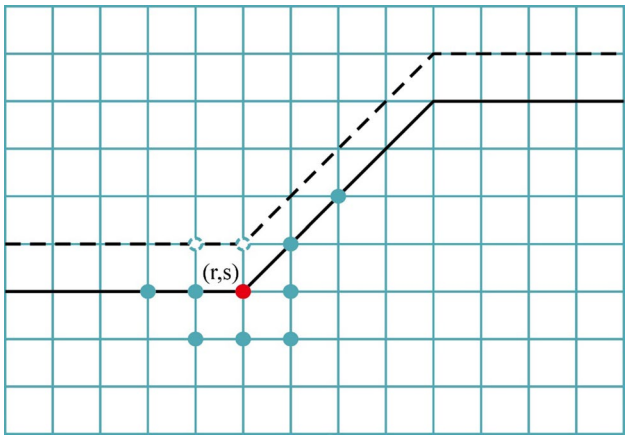

Fig. 5 Simulation point and discrete grid points used for the fourth case

where

$$
\begin{aligned}
c_{41} &= c_2\frac{1}{2}(1-\varepsilon_1)\frac{\lambda_{r-1,s}}{\eta_{r-1,s}}\frac{\Delta z}{2\Delta x} - d_1\frac{\lambda_{r-1,s}}{\eta_{r-1,s}}\frac{\Delta z}{2\Delta x},\\
c_{42} &= c_1 + c_4,\\
c_{43} &= c_7,\\
c_{44} &= c_2\left[(1-\varepsilon_0) - \frac{1}{2}(1-\varepsilon_1)\frac{\lambda_{r-1,s}}{\eta_{r-1,s}}\frac{\Delta z}{2\Delta x}\right] + c_5 + d_1\frac{\lambda_{r-1,s}}{\eta_{r-1,s}}\frac{\Delta z}{2\Delta x},\\
c_{45} &= c_8,\\
c_{46} &= -c_2\frac{1}{2}\varepsilon_1\frac{1}{2}\frac{\lambda_{r+1,s-2}}{\eta_{r+1,s-2}} + c_3,\\
c_{47} &= c_2\varepsilon_0 + c_6,\\
c_{48} &= c_9,\\
c_{49} &= c_2\frac{1}{2}\varepsilon_1\frac{1}{2}\frac{\lambda_{r+1,s-2}}{\eta_{r+1,s-2}},
\end{aligned}
\tag{21}
$$

$$
\begin{aligned}
d_{41} &= -c_1\frac{\Delta z}{2\Delta x},\\
d_{42} &= -c_2\frac{1}{2} + d_1,\\
d_{43} &= d_3,\\
d_{44} &= c_1\frac{\Delta z}{2\Delta x},\\
d_{45} &= 0,\\
d_{46} &= c_2\frac{1}{2}\left(1-\varepsilon_1\varepsilon_0'\right) + d_2,\\
d_{47} &= 0,\\
d_{48} &= d_4,\\
d_{49} &= c_2\frac{1}{2}\varepsilon_1\varepsilon_0',
\end{aligned}
\tag{22}
$$

and

$$
\begin{aligned}
\tilde{c}_{41} &= -\tilde{d}_1\frac{\lambda_{r-1,s}}{\eta_{r-1,s}}\frac{\Delta z}{2\Delta x},\\
\tilde{c}_{42} &= -\tilde{d}_2\frac{1}{2}\frac{\lambda_{r,s-1}}{\eta_{r,s-1}} + \tilde{c}_1,\\
\tilde{c}_{43} &= \tilde{c}_3,\\
\tilde{c}_{44} &= \tilde{d}_1\frac{\lambda_{r-1,s}}{\eta_{r-1,s}}\frac{\Delta z}{2\Delta x},\\
\tilde{c}_{45} &= 0,\\
\tilde{c}_{46} &= \tilde{d}_2\frac{1}{2}\frac{\lambda_{r,s-1}}{\eta_{r,s-1}}\left(1-\varepsilon_1\varepsilon_0'\right) + \tilde{c}_2,\\
\tilde{c}_{47} &= 0,\\
\tilde{c}_{48} &= \tilde{c}_4,\\
\tilde{c}_{49} &= \tilde{d}_2\frac{1}{2}\frac{\lambda_{r,s-1}}{\eta_{r,s-1}}\varepsilon_1\varepsilon_0',
\end{aligned}
\tag{23}
$$

$$
\begin{aligned}
\tilde{d}_{41} &= \tilde{d}_2\frac{1}{2}\frac{\lambda_{r,s-1}}{\eta_{r,s-1}}(1-\varepsilon_1)\frac{\Delta z}{2\Delta x} - \tilde{c}_1\frac{\Delta z}{2\Delta x},\\
\tilde{d}_{42} &= \tilde{d}_1 + \tilde{d}_4,\\
\tilde{d}_{43} &= \tilde{d}_7,\\
\tilde{d}_{44} &= \tilde{d}_2\left[(1-\varepsilon_0) - \frac{1}{2}\frac{\lambda_{r,s-1}}{\eta_{r,s-1}}(1-\varepsilon_1)\frac{\Delta z}{2\Delta x}\right] + \tilde{d}_5 + \tilde{c}_1\frac{\Delta z}{2\Delta x},\\
\tilde{d}_{45} &= \tilde{d}_8,\\
\tilde{d}_{46} &= -\tilde{d}_2\frac{1}{2}\frac{\lambda_{r,s-1}}{\eta_{r,s-1}}\varepsilon_1\frac{1}{2} + \tilde{d}_3,\\
\tilde{d}_{47} &= \tilde{d}_2\varepsilon_0 + \tilde{d}_6,\\
\tilde{d}_{48} &= \tilde{d}_9,\\
\tilde{d}_{49} &= \tilde{d}_2\frac{1}{2}\frac{\lambda_{r,s-1}}{\eta_{r,s-1}}\varepsilon_1\frac{1}{2}.
\end{aligned}
\tag{24}
$$

(5) Case 5

The simulation point in the fifth case is the slope-to-flat transition point in Fig. 6. Four discrete grid points are located outside the model when using the 9-point scheme. The numerical expressions at these points are introduced in "Appendix 1." The average-derivative difference operators are changed. We derive the new average-derivative scheme. Discrete grid points are the blue and red points in Fig. 6. We simplify the new numerical scheme by

$$\begin{cases} c_{51}u_{r-1,s+1} + c_{52}u_{r,s} + c_{53}u_{r,s+1} + c_{54}u_{r+1,s} + c_{55}u_{r+1,s+1} + c_{56}u_{r+2,s} \\ +d_{51}w_{r-1,s+1} + d_{52}w_{r,s} + d_{53}w_{r,s+1} + d_{54}w_{r+1,s} + d_{55}w_{r+1,s+1} + d_{56}w_{r+2,s} = 0, \\ \tilde{d}_{51}w_{r-1,s+1} + \tilde{d}_{52}w_{r,s} + \tilde{d}_{53}w_{r,s+1} + \tilde{d}_{54}w_{r+1,s} + \tilde{d}_{55}w_{r+1,s+1} + \tilde{d}_{56}w_{r+2,s} \\ +\tilde{c}_{51}u_{r-1,s+1} + \tilde{c}_{52}u_{r,s} + \tilde{c}_{53}u_{r,s+1} + \tilde{c}_{54}u_{r+1,s} + \tilde{c}_{55}u_{r+1,s+1} + \tilde{c}_{56}u_{r+2,s} = 0, \end{cases} \tag{25}$$

where

$$\begin{aligned} c_{51} &= c_2\frac{1}{2}(1-\varepsilon_{11})\frac{1}{2}\frac{\lambda_{r-1,s}}{\eta_{r-1,s}} + c_4\left(1-\varepsilon_0'\right) + c_7 - d_1\frac{1}{2}\frac{\lambda_{r-1,s-1}}{\eta_{r-1,s-1}}, \\ c_{52} &= c_1\left[1-\frac{1}{2}\frac{\lambda_{r+1,s}}{\eta_{r+1,s}}\frac{\Delta z}{2\Delta x}\right] + c_4\varepsilon_0' + c_5 - d_2\frac{\lambda_{r+1,s}}{\eta_{r+1,s}}\frac{\Delta z}{2\Delta x} \\ &\quad + c_2\left[(1-\varepsilon_{00}) - \frac{1}{2}\varepsilon_{11}\frac{\lambda_{r+1,s}}{\eta_{r+1,s}}\frac{\Delta z}{2\Delta x} - \frac{1}{2}(1-\varepsilon_{11})\frac{1}{2}\frac{\lambda_{r-1,s}}{\eta_{r-1,s}}\right], \\ c_{53} &= c_8, \\ c_{54} &= c_2\varepsilon_{00} + c_3 + c_6 + d_1\frac{1}{2}\frac{\lambda_{r-1,s-1}}{\eta_{r-1,s-1}}, \\ c_{55} &= c_9, \\ c_{56} &= c_1\frac{1}{2}\frac{\lambda_{r+1,s}}{\eta_{r+1,s}}\frac{\Delta z}{2\Delta x} + c_2\frac{1}{2}\varepsilon_{11}\frac{\lambda_{r+1,s}}{\eta_{r+1,s}}\frac{\Delta z}{2\Delta x} + d_2\frac{\lambda_{r+1,s}}{\eta_{r+1,s}}\frac{\Delta z}{2\Delta x}, \end{aligned} \tag{26}$$

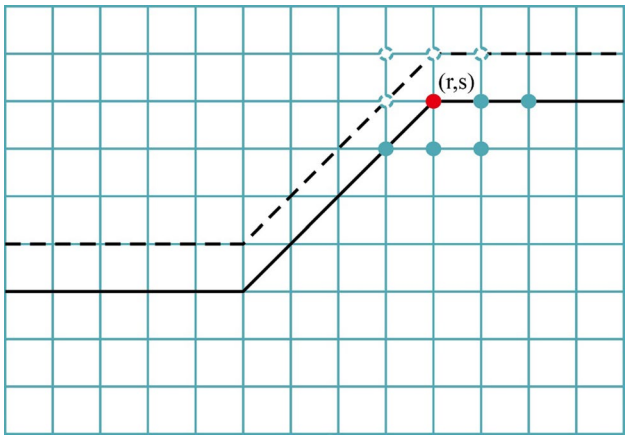

Fig. 6 Simulation point and discrete grid points used for the fifth case

$$\begin{aligned} d_{51} &= -c_1\frac{1}{2} - c_4\frac{1}{2} + d_3 \\ &\quad - c_2\frac{1}{2}\left[\varepsilon_{11} + (1-\varepsilon_{11})\left(1-\varepsilon_0'\right)\right], \\ d_{52} &= -c_2\frac{1}{2}(1-\varepsilon_{11})\varepsilon_0' - c_3\frac{\Delta z}{2\Delta x} \\ &\quad + c_4\frac{1}{2} + d_1\left[1-\frac{1}{2}\frac{\lambda_{r-1,s-1}}{\eta_{r-1,s-1}}\frac{\Delta z}{2\Delta x}\right], \\ d_{53} &= 0, \\ d_{54} &= c_1\frac{1}{2} + c_2\frac{1}{2} + d_2, \\ d_{55} &= d_4, \\ d_{56} &= c_3\frac{\Delta z}{2\Delta x} + d_1\frac{1}{2}\frac{\lambda_{r-1,s-1}}{\eta_{r-1,s-1}}\frac{\Delta z}{2\Delta x}, \end{aligned} \tag{27}$$

and

$$\begin{aligned} \tilde{c}_{51} &= -\tilde{d}_1\frac{1}{2}\frac{\lambda_{r-1,s-1}}{\eta_{r-1,s-1}} - \tilde{d}_4\frac{1}{2}\frac{\lambda_{r-1,s}}{\eta_{r-1,s}} + \tilde{c}_3 \\ &\quad - \tilde{d}_2\frac{1}{2}\frac{\lambda_{r,s-1}}{\eta_{r,s-1}}\left[\varepsilon_{11} + (1-\varepsilon_{11})\left(1-\varepsilon_0'\right)\right], \\ \tilde{c}_{52} &= -\tilde{d}_2\frac{1}{2}\frac{\lambda_{r,s-1}}{\eta_{r,s-1}}(1-\varepsilon_{11})\varepsilon_0' - \tilde{d}_3\frac{\lambda_{r+1,s}}{\eta_{r+1,s}}\frac{\Delta z}{2\Delta x} \\ &\quad + \tilde{d}_4\frac{1}{2}\frac{\lambda_{r-1,s}}{\eta_{r-1,s}} + \tilde{c}_1\left[1-\frac{1}{2}\frac{\lambda_{r+1,s}}{\eta_{r+1,s}}\frac{\Delta z}{2\Delta x}\right], \\ \tilde{c}_{53} &= 0, \\ \tilde{c}_{54} &= \tilde{d}_1\frac{1}{2}\frac{\lambda_{r-1,s-1}}{\eta_{r-1,s-1}} + \tilde{d}_2\frac{1}{2}\frac{\lambda_{r,s-1}}{\eta_{r,s-1}} + \tilde{c}_2, \\ \tilde{c}_{55} &= \tilde{c}_4, \\ \tilde{c}_{56} &= \tilde{d}_3\frac{\lambda_{r+1,s}}{\eta_{r+1,s}}\frac{\Delta z}{2\Delta x} + \tilde{c}_1\frac{1}{2}\frac{\lambda_{r+1,s}}{\eta_{r+1,s}}\frac{\Delta z}{2\Delta x}, \end{aligned} \tag{28}$$

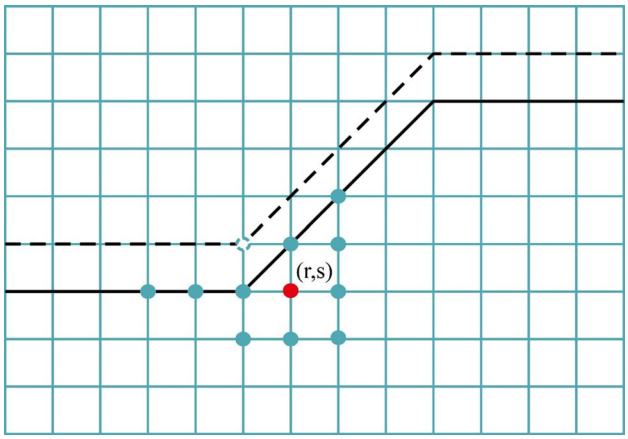

Fig. 7 Simulation point and discrete grid points used for the sixth case

$$
\begin{aligned}
\tilde{d}_{51} &= \tilde{d}_2\frac{1}{2}\frac{\lambda_{r,s-1}}{\eta_{r,s-1}}(1-\varepsilon_{11})\frac{1}{2}+\tilde{d}_4(1-\varepsilon_0')+\tilde{d}_7-\tilde{c}_1\frac{1}{2},\\
\tilde{d}_{52} &= \tilde{d}_1\left[1-\frac{1}{2}\frac{\lambda_{r-1,s-1}}{\eta_{r-1,s-1}}\frac{\Delta z}{2\Delta x}\right]+\tilde{d}_4\varepsilon_0'+\tilde{d}_5-\tilde{c}_2\frac{\Delta z}{2\Delta x}\\
&\quad+\tilde{d}_2\left[(1-\varepsilon_{00})-\frac{1}{2}\frac{\lambda_{r,s-1}}{\eta_{r,s-1}}\varepsilon_{11}\frac{\Delta z}{2\Delta x}-\frac{1}{2}\frac{\lambda_{r,s-1}}{\eta_{r,s-1}}(1-\varepsilon_{11})\frac{1}{2}\right],\\
\tilde{d}_{53} &= \tilde{d}_8,\\
\tilde{d}_{54} &= \tilde{d}_2\varepsilon_{00}+\tilde{d}_3+\tilde{d}_6+\tilde{c}_1\frac{1}{2},\\
\tilde{d}_{55} &= \tilde{d}_9,\\
\tilde{d}_{56} &= \tilde{d}_1\frac{1}{2}\frac{\lambda_{r-1,s-1}}{\eta_{r-1,s-1}}\frac{\Delta z}{2\Delta x}+\tilde{d}_2\frac{1}{2}\frac{\lambda_{r,s-1}}{\eta_{r,s-1}}\varepsilon_{11}\frac{\Delta z}{2\Delta x}+\tilde{c}_2\frac{\Delta z}{2\Delta x}.
\end{aligned}
\tag{29}
$$

(6) Case 6

The simulation point in the sixth case is the point on the right of the flat-to-slope transition point in Fig. 7. According to the 9-point scheme, one discrete grid point is located on the fiction line. The numerical expression at this point is given in "Appendix 1." Referring to this numerical expression, we derive the new average-derivative scheme. Discrete grid points are the blue and red points in Fig. 7. We simplify the new numerical scheme by

where

$$
\begin{aligned}
c_{61} &= c_1\frac{1}{2}(1-\varepsilon_1)\frac{\lambda_{r-2,s}}{\eta_{r-2,s}}\frac{\Delta z}{2\Delta x},\\
c_{62} &= -d_1\frac{1}{2}\frac{\lambda_{r-1,s-1}}{\eta_{r-1,s-1}},\\
c_{63} &= c_1\left[(1-\varepsilon_0)-\frac{1}{2}(1-\varepsilon_1)\frac{\lambda_{r-2,s}}{\eta_{r-2,s}}\frac{\Delta z}{2\Delta x}\right]+c_4,\\
c_{64} &= c_7,\\
c_{65} &= -c_1\frac{1}{2}\varepsilon_1\frac{1}{2}\frac{\lambda_{r,s-2}}{\eta_{r,s-2}}+c_2+d_1\frac{1}{2}\frac{\lambda_{r-1,s-1}}{\eta_{r-1,s-1}}\left(1-\varepsilon_1\varepsilon_0'\right),\\
c_{66} &= c_1\varepsilon_0+c_5,\\
c_{67} &= c_8,\\
c_{68} &= c_1\frac{1}{2}\varepsilon_1\frac{1}{2}\frac{\lambda_{r,s-2}}{\eta_{r,s-2}}+d_1\frac{1}{2}\frac{\lambda_{r-1,s-1}}{\eta_{r-1,s-1}}\varepsilon_1\varepsilon_0',\\
c_{69} &= c_3,\\
c_{610} &= c_6,\\
c_{611} &= c_9,
\end{aligned}
\tag{31}
$$

$$
\begin{aligned}
d_{61} &= d_1\frac{1}{2}\frac{\lambda_{r-1,s-1}}{\eta_{r-1,s-1}}(1-\varepsilon_1)\frac{\Delta z}{2\Delta x},\\
d_{62} &= -c_1\frac{1}{2},\\
d_{63} &= d_1\left[(1-\varepsilon_0)-\frac{1}{2}\frac{\lambda_{r-1,s-1}}{\eta_{r-1,s-1}}(1-\varepsilon_1)\frac{\Delta z}{2\Delta x}\right],\\
d_{64} &= d_3,\\
d_{65} &= c_1\frac{1}{2}(1-\varepsilon_1\varepsilon_0')-d_1\frac{1}{2}\frac{\lambda_{r-1,s-1}}{\eta_{r-1,s-1}}\varepsilon_1\frac{1}{2},\\
d_{66} &= d_1\varepsilon_0,\\
d_{67} &= 0,\\
d_{68} &= c_1\frac{1}{2}\varepsilon_1\varepsilon_0'+d_1\frac{1}{2}\frac{\lambda_{r-1,s-1}}{\eta_{r-1,s-1}}\varepsilon_1\frac{1}{2},\\
d_{69} &= d_2,\\
d_{610} &= 0,\\
d_{611} &= d_4,
\end{aligned}
\tag{32}
$$

and

$$
\begin{cases}
c_{61}u_{r-3,s}+c_{62}u_{r-2,s}+c_{63}u_{r-1,s}+c_{64}u_{r-1,s+1}+c_{65}u_{r,s-1}+c_{66}u_{r,s}\\
+c_{67}u_{r,s+1}+c_{68}u_{r+1,s-2}+c_{69}u_{r+1,s-1}+c_{610}u_{r+1,s}+c_{611}u_{r+1,s+1}\\
+d_{61}w_{r-3,s}+d_{62}w_{r-2,s}+d_{63}w_{r-1,s}+d_{64}w_{r-1,s+1}+d_{65}w_{r,s-1}+d_{66}w_{r,s}\\
+d_{67}w_{r,s+1}+d_{68}w_{r+1,s-2}+d_{69}w_{r+1,s-1}+d_{610}w_{r+1,s}+d_{611}w_{r+1,s+1}=0,\\
\tilde{d}_{61}w_{r-3,s}+\tilde{d}_{62}w_{r-2,s}+\tilde{d}_{63}w_{r-1,s}+\tilde{d}_{64}w_{r-1,s+1}+\tilde{d}_{65}w_{r,s-1}+\tilde{d}_{66}w_{r,s}\\
+\tilde{d}_{67}w_{r,s+1}+\tilde{d}_{68}w_{r+1,s-2}+\tilde{d}_{69}w_{r+1,s-1}+\tilde{d}_{610}w_{r+1,s}+\tilde{d}_{611}w_{r+1,s+1}\\
+\tilde{c}_{61}u_{r-3,s}+\tilde{c}_{62}u_{r-2,s}+\tilde{c}_{63}u_{r-1,s}+\tilde{c}_{64}u_{r-1,s+1}+\tilde{c}_{65}u_{r,s-1}+\tilde{c}_{66}u_{r,s}\\
+\tilde{c}_{67}u_{r,s+1}+\tilde{c}_{68}u_{r+1,s-2}+\tilde{c}_{69}u_{r+1,s-1}+\tilde{c}_{610}u_{r+1,s}+\tilde{c}_{611}u_{r+1,s+1}=0,
\end{cases}
\tag{30}
$$

$$
\begin{aligned}
\tilde{c}_{61} &= \tilde{c}_1 \frac{1}{2}(1-\varepsilon_1)\frac{\lambda_{r-2,s}}{\eta_{r-2,s}}\frac{\Delta z}{2\Delta x},\\
\tilde{c}_{62} &= -\tilde{d}_1 \frac{1}{2}\frac{\lambda_{r-1,s-1}}{\eta_{r-1,s-1}},\\
\tilde{c}_{63} &= \tilde{c}_1\left[(1-\varepsilon_0)-\frac{1}{2}(1-\varepsilon_1)\frac{\lambda_{r-2,s}}{\eta_{r-2,s}}\frac{\Delta z}{2\Delta x}\right],\\
\tilde{c}_{64} &= \tilde{c}_3,\\
\tilde{c}_{65} &= \tilde{d}_1 \frac{1}{2}\frac{\lambda_{r-1,s-1}}{\eta_{r-1,s-1}}\left(1-\varepsilon_1\varepsilon_0'\right)-\tilde{c}_1\frac{1}{2}\varepsilon_1\frac{1}{2}\frac{\lambda_{r,s-2}}{\eta_{r,s-2}},\\
\tilde{c}_{66} &= \tilde{c}_1\varepsilon_0,\\
\tilde{c}_{67} &= 0,\\
\tilde{c}_{68} &= \tilde{d}_1 \frac{1}{2}\frac{\lambda_{r-1,s-1}}{\eta_{r-1,s-1}}\varepsilon_1\varepsilon_0'+\tilde{c}_1\frac{1}{2}\varepsilon_1\frac{1}{2}\frac{\lambda_{r,s-2}}{\eta_{r,s-2}},\\
\tilde{c}_{69} &= \tilde{c}_2,\\
\tilde{c}_{610} &= 0,\\
\tilde{c}_{611} &= \tilde{c}_4,
\end{aligned}
\tag{33}
$$

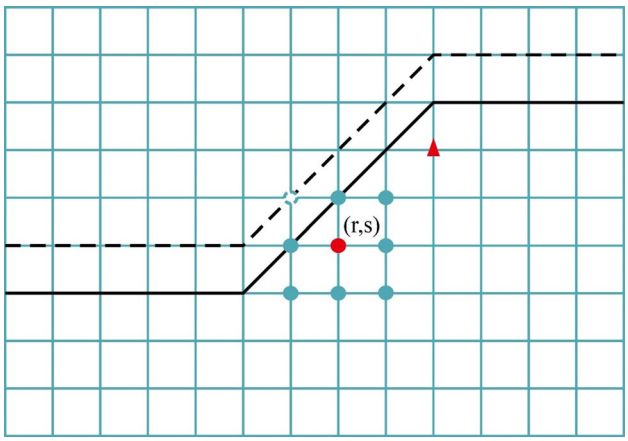

Fig. 8 Simulation points and discrete grid points used for the seventh case

$$
\begin{aligned}
\tilde{d}_{61} &= \tilde{d}_1 \frac{1}{2}\frac{\lambda_{r-1,s-1}}{\eta_{r-1,s-1}}(1-\varepsilon_1)\frac{\Delta z}{2\Delta x},\\
\tilde{d}_{62} &= -\tilde{c}_1\frac{1}{2},\\
\tilde{d}_{63} &= \tilde{d}_1\left[(1-\varepsilon_0)-\frac{1}{2}\frac{\lambda_{r-1,s-1}}{\eta_{r-1,s-1}}(1-\varepsilon_1)\frac{\Delta z}{2\Delta x}\right]+\tilde{d}_4,\\
\tilde{d}_{64} &= \tilde{d}_7,\\
\tilde{d}_{65} &= -\tilde{d}_1\frac{1}{2}\frac{\lambda_{r-1,s-1}}{\eta_{r-1,s-1}}\varepsilon_1\frac{1}{2}+\tilde{d}_2+\tilde{c}_1\frac{1}{2}\left(1-\varepsilon_1\varepsilon_0'\right),\\
\tilde{d}_{66} &= \tilde{d}_1\varepsilon_0+\tilde{d}_5,\\
\tilde{d}_{67} &= \tilde{d}_8,\\
\tilde{d}_{68} &= \tilde{d}_1\frac{1}{2}\frac{\lambda_{r-1,s-1}}{\eta_{r-1,s-1}}\varepsilon_1\frac{1}{2}+\tilde{c}_1\frac{1}{2}\varepsilon_1\varepsilon_0',\\
\tilde{d}_{69} &= \tilde{d}_3,\\
\tilde{d}_{610} &= \tilde{d}_6,\\
\tilde{d}_{611} &= \tilde{d}_9.
\end{aligned}
\tag{34}
$$

(7) Case 7

The simulation points in the seventh case are the red points under the slope in Fig. 8. If we use the conventional average-derivative scheme, one discrete grid point is located on the fiction line. The numerical expression at this point is given in "Appendix 1." The average-derivative difference operators are changed. We derive the new average-derivative scheme. Discrete grid points used by the new scheme are shown in Fig. 8 (the blue and red points). We simplify the new numerical scheme by

$$
\begin{cases}
c_{71}u_{r-1,s}+c_{72}u_{r-1,s+1}+c_{73}u_{r,s-1}+c_{74}u_{r,s}\\
+c_{75}u_{r,s+1}+c_{76}u_{r+1,s-1}+c_{77}u_{r+1,s}+c_{78}u_{r+1,s+1}\\
+d_{71}w_{r-1,s}+d_{72}w_{r-1,s+1}+d_{73}w_{r,s-1}+d_{74}w_{r,s}\\
+d_{75}w_{r,s+1}+d_{76}w_{r+1,s-1}+d_{77}w_{r+1,s}+d_{78}w_{r+1,s+1}=0,\\
\tilde{d}_{71}w_{r-1,s}+\tilde{d}_{72}w_{r-1,s+1}+\tilde{d}_{73}w_{r,s-1}+\tilde{d}_{74}w_{r,s}\\
+\tilde{d}_{75}w_{r,s+1}+\tilde{d}_{76}w_{r+1,s-1}+\tilde{d}_{77}w_{r+1,s}+\tilde{d}_{78}w_{r+1,s+1}\\
+\tilde{c}_{71}u_{r-1,s}+\tilde{c}_{72}u_{r-1,s+1}+\tilde{c}_{73}u_{r,s-1}+\tilde{c}_{74}u_{r,s}\\
+\tilde{c}_{75}u_{r,s+1}+\tilde{c}_{76}u_{r+1,s-1}+\tilde{c}_{77}u_{r+1,s}+\tilde{c}_{78}u_{r+1,s+1}=0,
\end{cases}
\tag{35}
$$

where

$$
\begin{aligned}
c_{71} &= c_1\left(1-\varepsilon_0'\right)+c_4-d_1\frac{1}{2}\frac{\lambda_{r-1,s-1}}{\eta_{r-1,s-1}},\\
c_{72} &= c_7,\\
c_{73} &= c_1\varepsilon_0'+c_2+d_1\frac{1}{2}\frac{\lambda_{r-1,s-1}}{\eta_{r-1,s-1}},\\
c_{74} &= c_5,\\
c_{75} &= c_8,\\
c_{76} &= c_3,\\
c_{77} &= c_6,\\
c_{78} &= c_9,
\end{aligned}
\tag{36}
$$

$$
\begin{aligned}
d_{71} &= -c_1\frac{1}{2}+d_1\left(1-\varepsilon_0'\right),\\
d_{72} &= d_3,\\
d_{73} &= c_1\frac{1}{2}+d_1\varepsilon_0',\\
d_{74} &= 0,\\
d_{75} &= 0,\\
d_{76} &= d_2,\\
d_{77} &= 0,\\
d_{78} &= d_4,
\end{aligned}
\tag{37}
$$

and

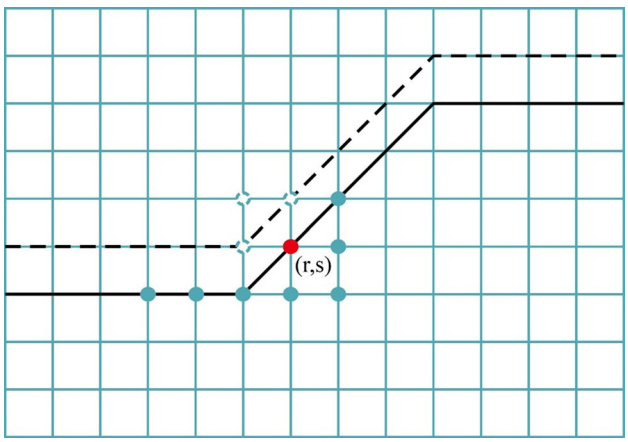

Fig. 9 Simulation point and discrete grid points used for the eighth case

$$
\begin{aligned}
\tilde{c}_{71} &= -\tilde{d}_1\frac{1}{2}\frac{\lambda_{r-1,s-1}}{\eta_{r-1,s-1}}+\tilde{c}_1\left(1-\varepsilon_0'\right),\\
\tilde{c}_{72} &= \tilde{c}_3,\\
\tilde{c}_{73} &= \tilde{d}_1\frac{1}{2}\frac{\lambda_{r-1,s-1}}{\eta_{r-1,s-1}}+\tilde{c}_1\varepsilon_0',\\
\tilde{c}_{74} &= 0,\\
\tilde{c}_{75} &= 0,\\
\tilde{c}_{76} &= \tilde{c}_2,\\
\tilde{c}_{77} &= 0,\\
\tilde{c}_{78} &= \tilde{c}_4,
\end{aligned}
\tag{38}
$$

$$
\begin{aligned}
\tilde{d}_{71} &= \tilde{d}_1\left(1-\varepsilon_0'\right)+\tilde{d}_4-\tilde{c}_1\frac{1}{2},\\
\tilde{d}_{72} &= \tilde{d}_7,\\
\tilde{d}_{73} &= \tilde{d}_1\varepsilon_0'+\tilde{d}_2+\tilde{c}_1\frac{1}{2},\\
\tilde{d}_{74} &= \tilde{d}_5,\\
\tilde{d}_{75} &= \tilde{d}_8,\\
\tilde{d}_{76} &= \tilde{d}_3,\\
\tilde{d}_{77} &= \tilde{d}_6,\\
\tilde{d}_{78} &= \tilde{d}_9.
\end{aligned}
\tag{39}
$$

(8) Case 8

The simulation point in the eighth case is the point on the slope which is next to the flat-to-slope transition point (Fig. 9). Three discrete grid points are outside the model when using the 9-point scheme. The numerical expressions at these points are given in "Appendix 1." We derive the new average-derivative scheme by these numerical expressions. Discrete grid points used by the new scheme are shown in Fig. 9 (the blue and red points). We simplify the new numerical scheme by

$$
\begin{cases}
c_{81}u_{r-3,s+1}+c_{82}u_{r-2,s+1}+c_{83}u_{r-1,s+1}+c_{84}u_{r,s}\\
+c_{85}u_{r,s+1}+c_{86}u_{r+1,s-1}+c_{87}u_{r+1,s}+c_{88}u_{r+1,s+1}\\
+d_{81}w_{r-3,s+1}+d_{82}w_{r-2,s+1}+d_{83}w_{r-1,s+1}+d_{84}w_{r,s}\\
+d_{85}w_{r,s+1}+d_{86}w_{r+1,s-1}+d_{87}w_{r+1,s}+d_{88}w_{r+1,s+1}=0,\\
\tilde{d}_{81}w_{r-3,s+1}+\tilde{d}_{82}w_{r-2,s+1}+\tilde{d}_{83}w_{r-1,s+1}+\tilde{d}_{84}w_{r,s}\\
+\tilde{d}_{85}w_{r,s+1}+\tilde{d}_{86}w_{r+1,s-1}+\tilde{d}_{87}w_{r+1,s}+\tilde{d}_{88}w_{r+1,s+1}\\
+\tilde{c}_{81}u_{r-3,s+1}+\tilde{c}_{82}u_{r-2,s+1}+\tilde{c}_{83}u_{r-1,s+1}+\tilde{c}_{84}u_{r,s}\\
+\tilde{c}_{85}u_{r,s+1}+\tilde{c}_{86}u_{r+1,s-1}+\tilde{c}_{87}u_{r+1,s}+\tilde{c}_{88}u_{r+1,s+1}=0,
\end{cases}
\tag{40}
$$

where

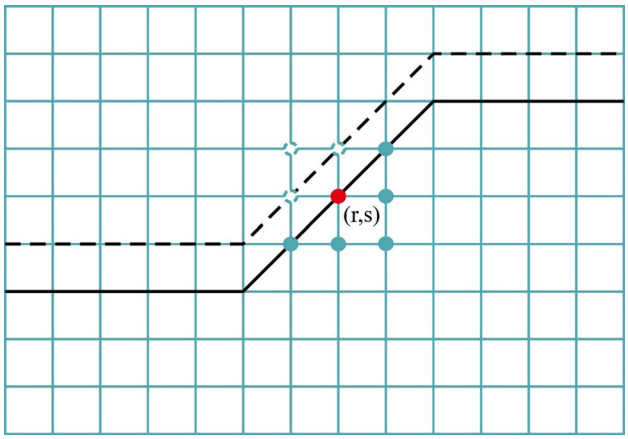

Fig. 10 Simulation points and discrete grid points used for the ninth case

$$
\begin{aligned}
c_{81} &= c_4\frac{1}{2}(1-\varepsilon_1)\frac{\lambda_{r-2,s+1}}{\eta_{r-2,s+1}}\frac{\Delta z}{2\Delta x},\\
c_{82} &= 0,\\
c_{83} &= c_4\left[(1-\varepsilon_0)-\frac{1}{2}(1-\varepsilon_1)\frac{\lambda_{r-2,s+1}}{\eta_{r-2,s+1}}\frac{\Delta z}{2\Delta x}\right]+c_7-d_1\frac{1}{2}\frac{\lambda_{r-1,s-1}}{\eta_{r-1,s-1}},\\
c_{84} &= c_1+c_2(1-\varepsilon_0')-c_4\frac{1}{2}\varepsilon_1\frac{1}{2}\frac{\lambda_{r,s-1}}{\eta_{r,s-1}}+c_5,\\
c_{85} &= c_4\varepsilon_0+c_8,\\
c_{86} &= c_2\varepsilon_0'+c_3+c_4\frac{1}{2}\varepsilon_1\frac{1}{2}\frac{\lambda_{r,s-1}}{\eta_{r,s-1}}+d_1\frac{1}{2}\frac{\lambda_{r-1,s-1}}{\eta_{r-1,s-1}},\\
c_{87} &= c_6,\\
c_{88} &= c_9,
\end{aligned}
\tag{41}
$$

$$
\begin{aligned}
d_{81} &= 0,\\
d_{82} &= -c_4\frac{1}{2},\\
d_{83} &= -c_1\frac{1}{2}+d_3,\\
d_{84} &= -c_2\frac{1}{2}+c_4\frac{1}{2}\left(1-\varepsilon_1\varepsilon_0'\right)+d_1,\\
d_{85} &= 0,\\
d_{86} &= c_1\frac{1}{2}+c_2\frac{1}{2}+c_4\frac{1}{2}\varepsilon_1\varepsilon_0'+d_2,\\
d_{87} &= 0,\\
d_{88} &= d_4,
\end{aligned}
\tag{42}
$$

and

$$
\begin{aligned}
\tilde{c}_{81} &= 0,\\
\tilde{c}_{82} &= -\tilde{d}_4\frac{1}{2}\frac{\lambda_{r-1,s}}{\eta_{r-1,s}},\\
\tilde{c}_{83} &= -\tilde{d}_1\frac{1}{2}\frac{\lambda_{r-1,s-1}}{\eta_{r-1,s-1}}+\tilde{c}_3,\\
\tilde{c}_{84} &= -\tilde{d}_2\frac{1}{2}\frac{\lambda_{r,s-1}}{\eta_{r,s-1}}+\tilde{d}_4\frac{1}{2}\frac{\lambda_{r-1,s}}{\eta_{r-1,s}}\left(1-\varepsilon_1\varepsilon_0'\right)+\tilde{c}_1,\\
\tilde{c}_{85} &= 0,\\
\tilde{c}_{86} &= \tilde{d}_1\frac{1}{2}\frac{\lambda_{r-1,s-1}}{\eta_{r-1,s-1}}+\tilde{d}_2\frac{1}{2}\frac{\lambda_{r,s-1}}{\eta_{r,s-1}}+\tilde{d}_4\frac{1}{2}\frac{\lambda_{r-1,s}}{\eta_{r-1,s}}\varepsilon_1\varepsilon_0'+\tilde{c}_2,\\
\tilde{c}_{87} &= 0,\\
\tilde{c}_{88} &= \tilde{c}_4,
\end{aligned}
\tag{43}
$$

$$
\begin{aligned}
\tilde{d}_{81} &= \tilde{d}_4\frac{1}{2}\frac{\lambda_{r-1,s}}{\eta_{r-1,s}}(1-\varepsilon_1)\frac{\Delta z}{2\Delta x},\\
\tilde{d}_{82} &= 0,\\
\tilde{d}_{83} &= \tilde{d}_4\left[(1-\varepsilon_0)-\frac{1}{2}\frac{\lambda_{r-1,s}}{\eta_{r-1,s}}(1-\varepsilon_1)\frac{\Delta z}{2\Delta x}\right]+\tilde{d}_7-\tilde{c}_1\frac{1}{2},\\
\tilde{d}_{84} &= \tilde{d}_1+\tilde{d}_2\left(1-\varepsilon_0'\right)-\tilde{d}_4\frac{1}{2}\frac{\lambda_{r-1,s}}{\eta_{r-1,s}}\varepsilon_1\frac{1}{2}+\tilde{d}_5,\\
\tilde{d}_{85} &= \tilde{d}_4\varepsilon_0+\tilde{d}_8,\\
\tilde{d}_{86} &= \tilde{d}_2\varepsilon_0'+\tilde{d}_3+\tilde{d}_4\frac{1}{2}\frac{\lambda_{r-1,s}}{\eta_{r-1,s}}\varepsilon_1\frac{1}{2}+\tilde{c}_1\frac{1}{2},\\
\tilde{d}_{87} &= \tilde{d}_6,\\
\tilde{d}_{88} &= \tilde{d}_9.
\end{aligned}
\tag{44}
$$

(9) Case 9

The simulation points in the ninth case are points on the slope in Fig. 10. There are three discrete grid points outside the model when using the 9-point scheme. The numerical expressions at these points are introduced in "Appendix 1." With these numerical expressions, we derive the new average-derivative scheme. The average-derivative difference operators are changed. Discrete grid points we used are shown in Fig. 10 (the blue and red points). We simplify the new numerical scheme by

$$
\begin{cases}
c_{91}u_{r-1,s+1}+c_{92}u_{r,s}+c_{93}u_{r,s+1}+c_{94}u_{r+1,s-1}+c_{95}u_{r+1,s}+c_{96}u_{r+1,s+1}\\
+d_{91}w_{r-1,s+1}+d_{92}w_{r,s}+d_{93}w_{r,s+1}+d_{94}w_{r+1,s-1}+d_{95}w_{r+1,s}+d_{96}w_{r+1,s+1}=0,\\
\tilde{d}_{91}w_{r-1,s+1}+\tilde{d}_{92}w_{r,s}+\tilde{d}_{93}w_{r,s+1}+\tilde{d}_{94}w_{r+1,s-1}+\tilde{d}_{95}w_{r+1,s}+\tilde{d}_{96}w_{r+1,s+1}\\
+\tilde{c}_{91}u_{r-1,s+1}+\tilde{c}_{92}u_{r,s}+\tilde{c}_{93}u_{r,s+1}+\tilde{c}_{94}u_{r+1,s-1}+\tilde{c}_{95}u_{r+1,s}+\tilde{c}_{96}u_{r+1,s+1}=0,
\end{cases}
\tag{45}
$$

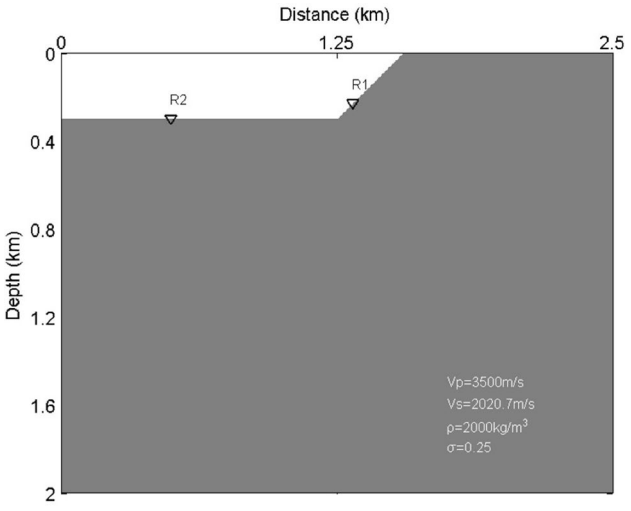

Fig. 11 A 2D homogeneous model with a slope free surface. Inverted triangles on the free surface represent the receivers R1 and R2

where

$$
\begin{aligned}
c_{91} &= c_4\left(1-\varepsilon_0'\right)+c_7-d_1\frac{1}{2}\frac{\lambda_{r-1,s-1}}{\eta_{r-1,s-1}},\\
c_{92} &= c_1+c_2\left(1-\varepsilon_0'\right)+c_4\varepsilon_0'+c_5,\\
c_{93} &= c_8,\\
c_{94} &= c_2\varepsilon_0'+c_3+d_1\frac{1}{2}\frac{\lambda_{r-1,s-1}}{\eta_{r-1,s-1}},\\
c_{95} &= c_6,\\
c_{96} &= c_9,
\end{aligned}
\tag{46}
$$

$$
\begin{aligned}
d_{91} &= -c_1\frac{1}{2}-c_4\frac{1}{2}+d_3,\\
d_{92} &= -c_2\frac{1}{2}+c_4\frac{1}{2}+d_1,\\
d_{93} &= 0,\\
d_{94} &= c_1\frac{1}{2}+c_2\frac{1}{2}+d_2,\\
d_{95} &= 0,\\
d_{96} &= d_4,
\end{aligned}
\tag{47}
$$

and

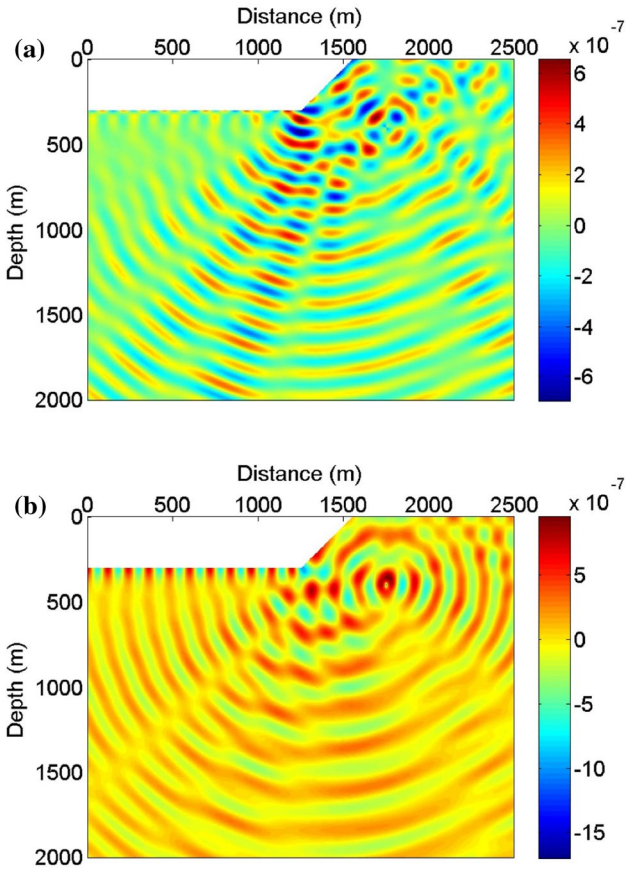

Fig. 12 Elastic wave field at frequency 19.1 Hz. **a** Horizontal component and **b** vertical component

$$
\begin{aligned}
\tilde{c}_{91} &= -\tilde{d}_1\frac{1}{2}\frac{\lambda_{r-1,s-1}}{\eta_{r-1,s-1}}-\tilde{d}_4\frac{1}{2}\frac{\lambda_{r-1,s}}{\eta_{r-1,s}}+\tilde{c}_3,\\
\tilde{c}_{92} &= -\tilde{d}_2\frac{1}{2}\frac{\lambda_{r,s-1}}{\eta_{r,s-1}}+\tilde{d}_4\frac{1}{2}\frac{\lambda_{r-1,s}}{\eta_{r-1,s}}+\tilde{c}_1,\\
\tilde{c}_{93} &= 0,\\
\tilde{c}_{94} &= \tilde{d}_1\frac{1}{2}\frac{\lambda_{r-1,s-1}}{\eta_{r-1,s-1}}+\tilde{d}_2\frac{1}{2}\frac{\lambda_{r,s-1}}{\eta_{r,s-1}}+\tilde{c}_2,\\
\tilde{c}_{95} &= 0,\\
\tilde{c}_{96} &= \tilde{c}_4,
\end{aligned}
\tag{48}
$$

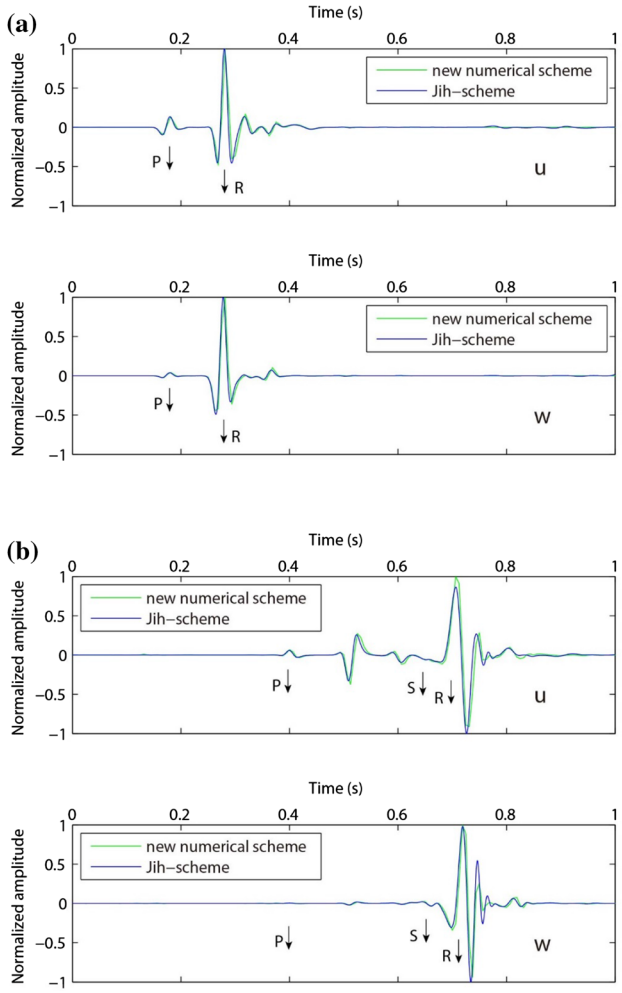

Fig. 13 Seismograms at different receivers: **a** the receiver R1 and **b** the receiver R2. Green line and blue line represent the results computed by our frequency-domain method plus Fourier transformation and Jih's time-domain method, respectively

$$
\begin{aligned}
\tilde{d}_{91} &= \tilde{d}_4\left(1-\varepsilon_0'\right)+\tilde{d}_7-\tilde{c}_1\frac{1}{2},\\
\tilde{d}_{92} &= \tilde{d}_1+\tilde{d}_2\left(1-\varepsilon_0'\right)+\tilde{d}_4\varepsilon_0'+\tilde{d}_5,\\
\tilde{d}_{93} &= \tilde{d}_8,\\
\tilde{d}_{94} &= \tilde{d}_2\varepsilon_0'+\tilde{d}_3+\tilde{c}_1\frac{1}{2},\\
\tilde{d}_{95} &= \tilde{d}_6,\\
\tilde{d}_{96} &= \tilde{d}_9.
\end{aligned}
\tag{49}
$$

Feasibility analysis

To test the feasibility of our method, we design a model with a simple irregular free surface. There is a 45° slope on the free surface. The dimensions of the model are 2.5 km × 2.0 km with the grid spacing of $\Delta x = \Delta z = 2.5$ m. The two transition points of the free surface are at (0.3 km, 1.25 km) and (0 km, 1.55 km), respectively. Two flats are located at depth 0.3 km and 0 km, respectively (Fig. 11). Except for the free surface, the remaining three boundaries are handled with the PML boundary conditions. The velocities of the P-wave and S-wave are 3500 m/s, and 2020.7 m/s, respectively. We use a density of 2000 kg/m^3 and a Poisson ratio of 0.25. Here, we use a point source applied to the vertical displacement at (0.4 km, 1.75 km). The source function is the Ricker wavelet with a peak frequency of 30 Hz.

Figure 12 shows the frequency-domain seismic wave field for the frequency of 19.1 Hz. It involves two components of the real part of displacement, namely horizontal (Fig. 12a) and vertical (Fig. 12b). The elastic wave field for the model with irregular surface can be simulated by our method. Figure 13 shows the particle displacement at receivers as shown in Fig. 11. The symbols *P*, *S* and *R* in Fig. 13 represent the *P*-wave, *S*-wave and Rayleigh wave, respectively. From Fig. 13a, only the *P*-wave and Rayleigh wave can be recognized. The reason why the *S*-wave cannot be recognized at a small offset is that travel times of the *S*-wave and Rayleigh wave are approximate and the energy of Rayleigh wave is much stronger than *S*-wave. At a large offset, we can recognize the *P*-wave, *S*-wave and Rayleigh wave in Fig. 13b. The disturbance in the seismograms calculated by our method and Jih's time-domain method may be caused by artificial diffraction produced at the corner. The tiny disturbance has no impact for us to obtain the conclusion. The results in Fig. 13 are computed by our method and Jih's time-domain method. These two results agree with each other well. The good agreement with Jih's time-domain solution demonstrates the feasibility of our method.

Figure 14 shows the structure of the impedance matrix when using the rigid boundary condition. The rigid boundary condition means that the displacements are zero on the fiction line. In order to describe the structure clearly, we rebuild a model similar to Fig. 11 except for the size. As we know, nonzero entries distribute on the diagonal of the impedance matrix when modeling with the flat free surface. According to Fig. 14a, entries along the diagonal are still nonzero. Figure 14b and c shows the structure in some parts in detail. We can see that the shape of the free surface has influence on the distribution of nonzero entries. Figure 15a is the structure of the matrix when using the free-surface boundary condition. Nonzero entries are still along the diagonals. Figure 15b and c shows the details of some parts of the matrix. Compared to Fig. 14, Fig. 15 shows that the matrix structure is affected not only by the shape of topographies but also by the discretization of the wave equation on the free surface.

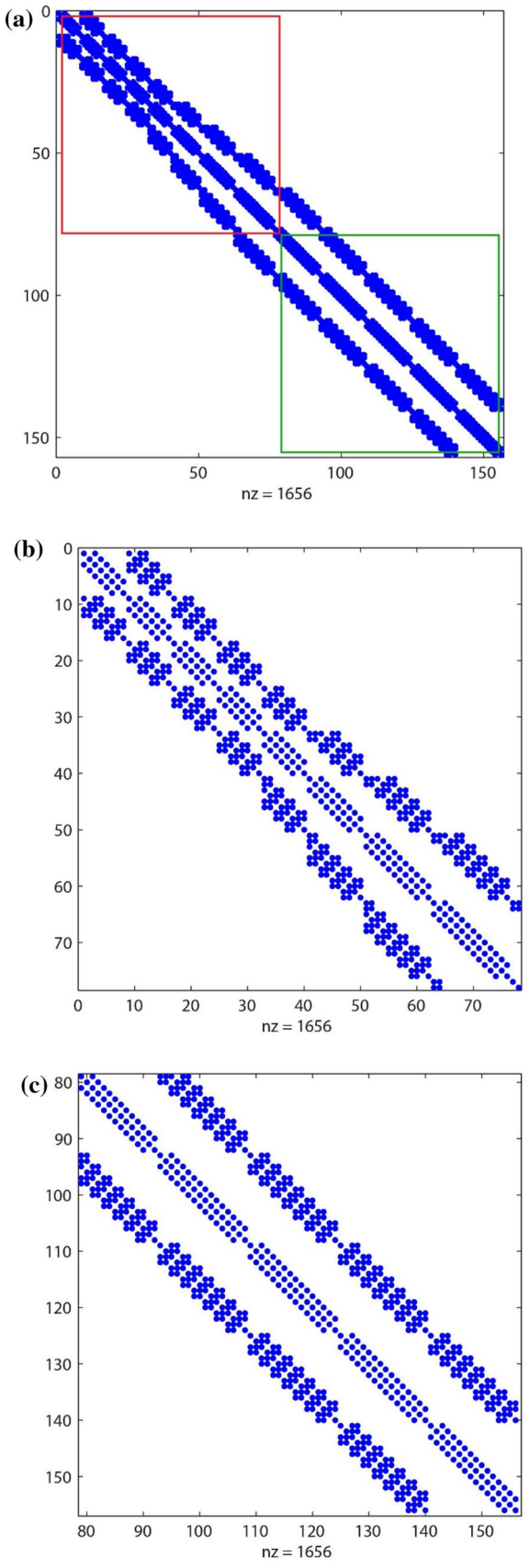

Fig. 14 Impedance matrix structure with the ridged boundary condition. **a** Distribution of the nonzero entries in the whole matrix, **b** distribution of the nonzero entries in the red rectangle and **c** distribution of the nonzero entries in the green rectangle

Numerical examples

We now perform numerical experiments on models with a more complex free surface. First, we build a model with irregular topography similar to a valley. Figure 16 shows the model. The dimensions of the model are also 2.5 km × 2.0 km, and the spatial intervals Δx and Δz are both 2.5 m. We place four transition points separately at (0 km, 0.7 km), (0.3 km, 1 km), (0.3 km, 1.5 km) and (0 km, 1.8 km). The depths of three flats are 0 km, 0.3 km and 0 km, respectively. The other three boundaries are still dealt with the PML boundary conditions. The P-wave velocity, the S-wave velocity, the Poisson ratio and the density are still 3500 m/s, 2020.7 m/s, 0.25 and 2000 kg/m^3, respectively. The point source applied to the vertical displacement is at (0.4 km, 0.6 km), and the source signal is the Ricker wavelet with a peak frequency of 30 Hz.

For the frequency of 19.1 Hz, we show the u (Fig. 17a) and w (Fig. 17b) components of the displacements. To validate our method, we extract particle displacement at receivers shown in Fig. 16. Figures 18a–c shows the results at receivers R1–R3, respectively. From Fig. 18, we observe that the P-wave, S-wave and Rayleigh wave are simulated clearly using our method. They are indicated by arrows in Fig. 18. There is a little tiny disturbance in the seismograms calculated by our method and Jih's time-domain method. They are caused by the artificial diffraction at corners probably. The tiny disturbance has no impact for us to obtain the conclusion. We also make a comparison between our method and Jih's time-domain method (Fig. 18). According to the comparison between the green line and the blue line at all receivers, computation result with our method can match the result of Jih's time-domain method very well except for the tiny amplitude error at peak position which is caused by different numerical schemes. This test proves that our method is also available to a more complex topography.

To be close to the real terrain, we build a more complex free surface with both a valley and a ridge. This model is shown in Fig. 19. The size is still 2.5 km × 2.0 km with a grid interval of 2.5 m. There are eight transition points, and their positions are (0.05 km, 0.4 km), (0 km, 0.45 km), (0 km, 0.85 km), (0.05 km, 0.9 km), (0.05 km, 1.5 km), (0.1 km, 1.55 km), (0.1 km, 2.05 km) and (0.05 km, 2.1 km), respectively. The depths of three kinds of flat surfaces are 0 km, 0.05 km and 0.1 km, respectively. The P-wave velocity and the density are still 3500 m/s and 2000 kg/m^3. The Poisson ratio is 0.25 and the corresponding S-wave velocity is 2020.7 m/s. The source time function is expressed by

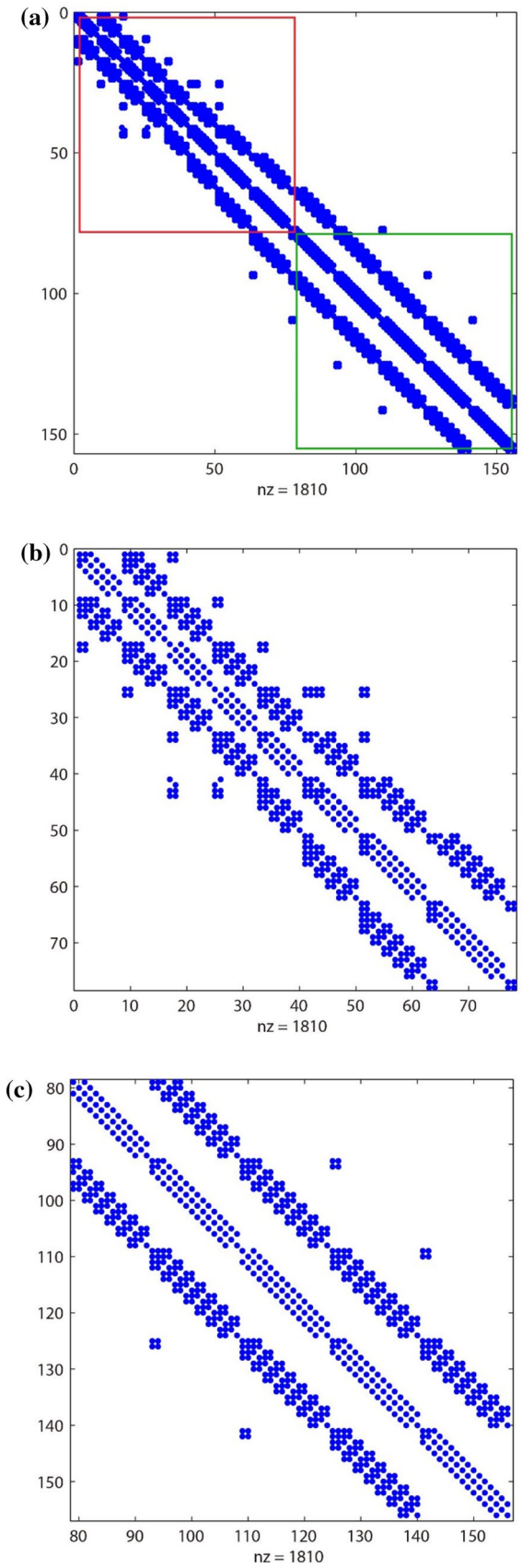

Fig. 15 Impedance matrix structure with the free-surface boundary condition. **a** Distribution of the nonzero entries in the whole matrix, **b** distribution of the nonzero entries in the red rectangle and **c** distribution of the nonzero entries in the green rectangle

Ricker wavelet with 30 Hz as the peak frequency. The position of the point source applied to the vertical displacement is changed to (0.15 km, 0.5 km).

For comparison, we still simulate the wave field at the frequency of 19.1 Hz. Figure 20 shows the horizontal and vertical components of the displacements. To provide more information, we extract particle displacement at R1 in Fig. 19. The *P*-wave, *S*-wave and Rayleigh wave are indicated by arrows in Fig. 21. They are still simulated successfully by our method for more complicated irregular free surface. From Fig. 21, it can be seen that a good agreement between the results of the proposed method and Jih's time-domain method is achieved, especially for the phases. Therefore, the feasibility of the proposed method is approved in the modeling case of complex irregular topography. The tiny amplitude errors at the peak have no impact for us to demonstrate that our method can be applied with complex topographies.

Conclusion

Based on a local rotated coordinate method and an average-derivative optimal approach, we proposed a new average-derivative scheme for implementing the irregular topography in the frequency domain. This technique specifies the treatment to the polygonal topography. We illustrated the idea of our method by a simple model with a 45° slope. The irregular free surface is decomposed into nine parts. We generalized the conventional average-derivative difference operator to the rotated coordinate aligned with the irregular free surface using a local rotated coordinate method and derived new average-derivative difference schemes on irregular topography in the frequency domain. Numerical experiments with this simple model demonstrate the feasibility of our method. We analyzed the factors affecting the structure of impedance matrix. These factors include the shape of the free surface and the format of discrete equations. We further demonstrated the effectiveness of our method with more complicated topographies. The conventional average-derivative optimal method is an accurate frequency-domain simulation scheme with a relatively low computational cost. Previously, it can only be applied to models with a horizontal free surface. Using our new scheme, the average-derivative optimal method can be applied to models with an irregular free surface.

Acknowledgements We would like to express our sincere appreciation to Associate Editor Dr. Sanyi Yuan and two reviewers for their insightful comments and valuable suggestions, which have greatly helped us

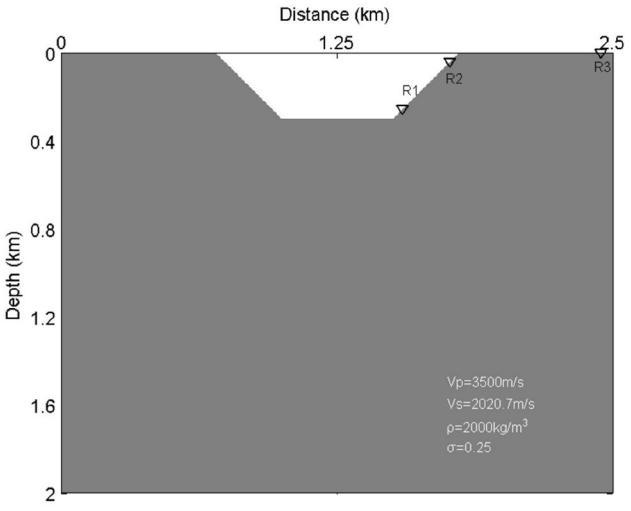

Fig. 16 A 2D homogeneous model with a valley-shaped free surface. Receivers R1, R2 and R3 are denoted by reversed triangles

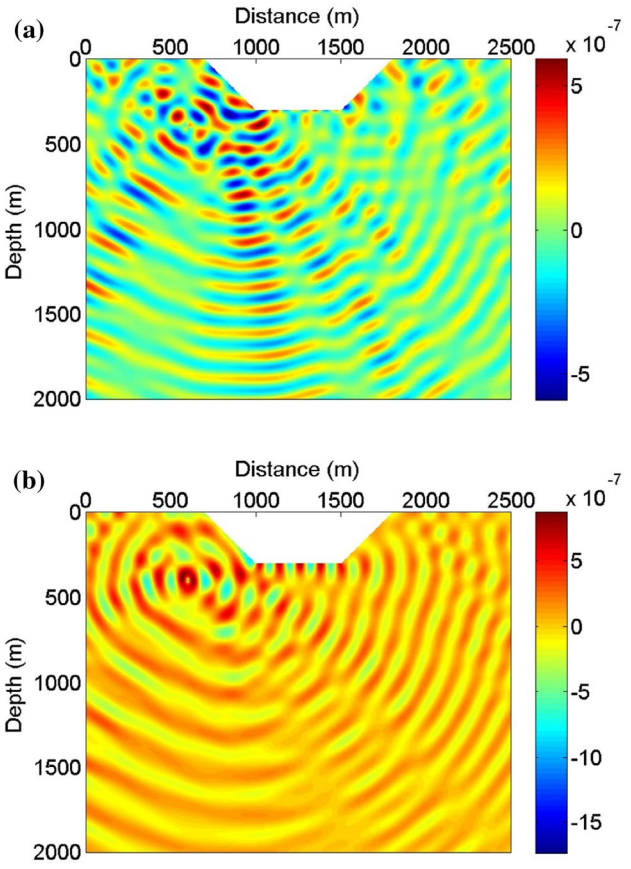

Fig. 17 Elastic wave field at frequency 19.1 Hz. **a** Horizontal component and **b** vertical component

in the improvement in the paper. This work is supported by National Natural Science Foundation of China under Grant Nos. 41874163 and 41674132.

Appendix 1: The local rotated coordinate method in frequency domain

According to Fig. 1, the free surface is composed by three segments. We deal with the free-surface boundary condition at flat, slope and transition points, respectively. Following Jih et al. (1988), we derive expressions of the free-surface boundary condition in frequency domain for the following cases:

1. Flat

The free-surface boundary condition satisfies the stress-free condition. According to Eq. (1), we have

$$\begin{cases} \tau_{xz} = \mu\left(\frac{\partial u}{\partial z} + \frac{\partial w}{\partial x}\right) = 0, \\ \tau_{zz} = (\lambda + 2\mu)\frac{\partial w}{\partial z} + \lambda\frac{\partial u}{\partial x} = 0. \end{cases} \tag{50}$$

We rewrite Eq. (50) as

$$\begin{cases} \frac{\partial u}{\partial z} + \frac{\partial w}{\partial x} = 0, \\ \eta\frac{\partial w}{\partial z} + \lambda\frac{\partial u}{\partial x} = 0. \end{cases} \tag{51}$$

Using one-side approximate approach to discretize Eq. (51), we have the expression of the flat free-surface boundary condition (Fig. 22):

$$\begin{cases} u_{r,s} = u_{r,s+1} + \frac{\Delta z}{2\Delta x}(w_{r+1,s+1} - w_{r-1,s+1}), \\ w_{r,s} = w_{r,s+1} + \frac{\lambda_{r,s+1}}{\eta_{r,s+1}}\frac{\Delta z}{2\Delta x}(u_{r+1,s+1} - u_{r-1,s+1}). \end{cases} \tag{52}$$

2. Slope

We represent new x-axis and z-axis by x' and z'. Similar to the flat case, we consider Eq. (50) in the new coordinate system (Fig. 23); the expression of Eq. (51) changes to

$$\begin{cases} \frac{\partial u'}{\partial z'} + \frac{\partial w'}{\partial x'} = 0, \\ \frac{\partial w'}{\partial z'} + \frac{\lambda}{\eta}\frac{\partial u'}{\partial x'} = 0, \end{cases} \tag{53}$$

where u' and w' are horizontal and vertical components of displacement in the new coordinate system. Choosing grid points in Fig. 23 to discretize Eq. (53), we have

$$\begin{cases} \frac{u'_0 - u'_{r,s}}{\Delta z'} + \frac{w'_{r+1,s} - w'_{r,s+1}}{\Delta x'} = 0, \\ \frac{w'_0 - w'_{r,s}}{\Delta z'} + \frac{\lambda_{r,s}}{\eta_{r,s}}\frac{u'_{r+1,s} - u'_{r,s+1}}{\Delta x'} = 0, \end{cases} \tag{54}$$

where

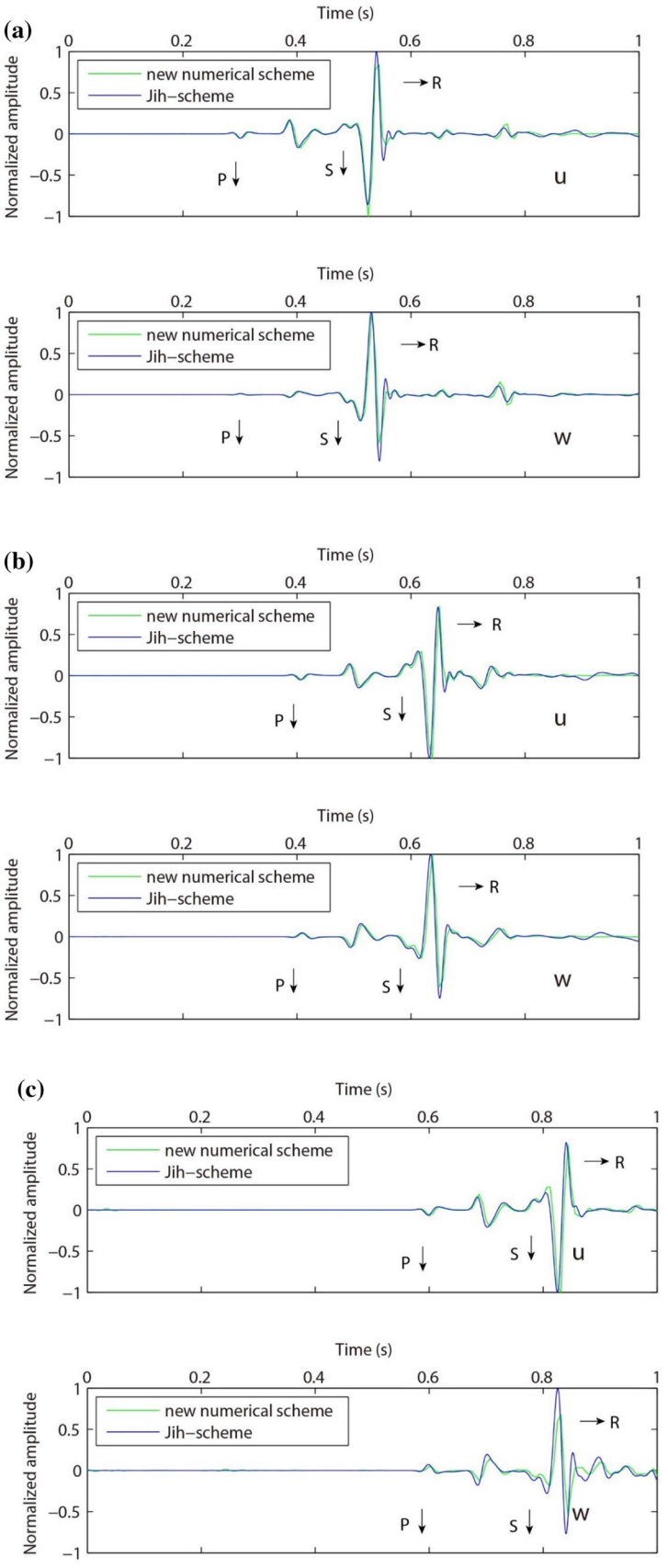

Fig. 18 Seismograms at receivers R1–R3: **a** receiver R1; **b** receiver R2; **c** receiver R3. Green line and blue line represent the results computed by our frequency-domain method plus Fourier transformation and Jih's time-domain method, respectively

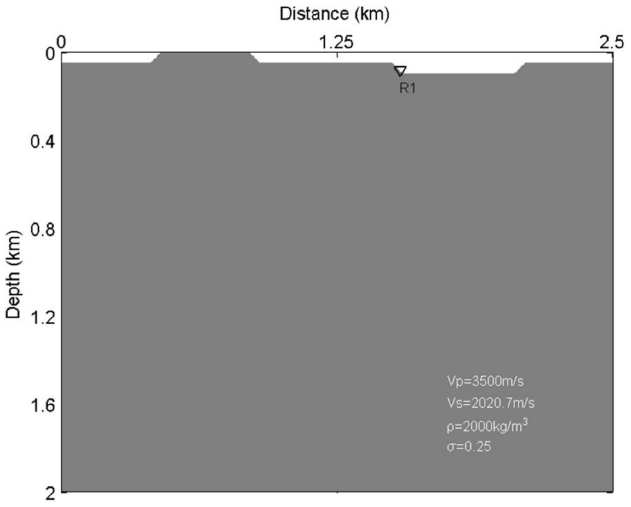

Fig. 19 A 2D homogeneous model with a valley-ridge-shaped free surface. The reversed triangle denotes the receiver R1

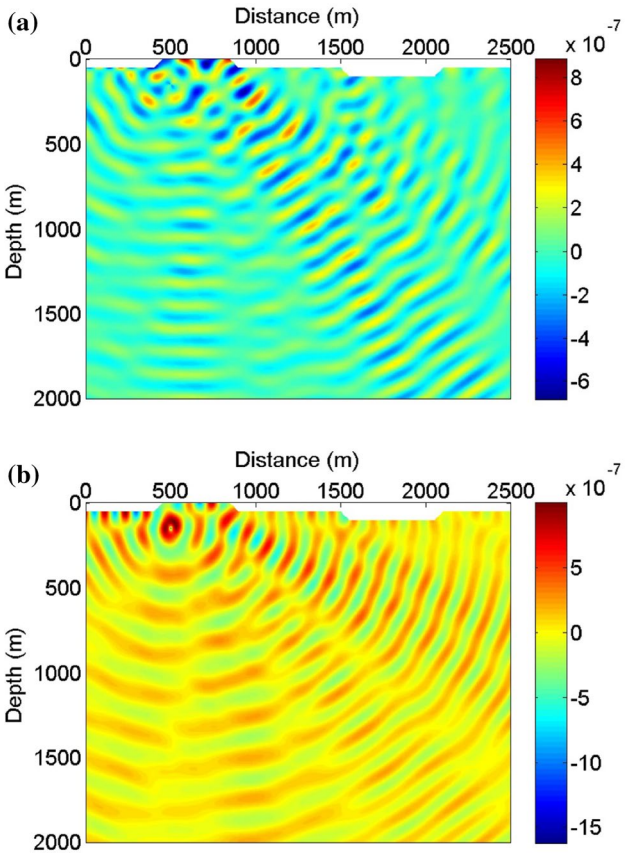

Fig. 20 Elastic wave field at frequency 19.1 Hz. **a** Horizontal component and **b** vertical component

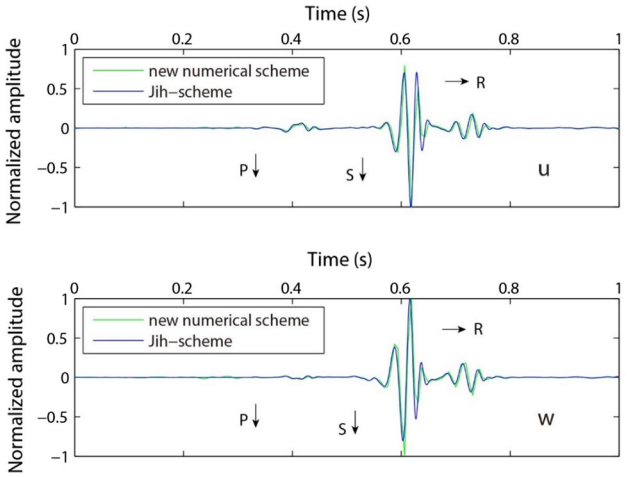

Fig. 21 Seismograms at receiver R1. Green line and blue line represent the results computed by our frequency-domain method plus Fourier transformation and Jih's time-domain method, respectively

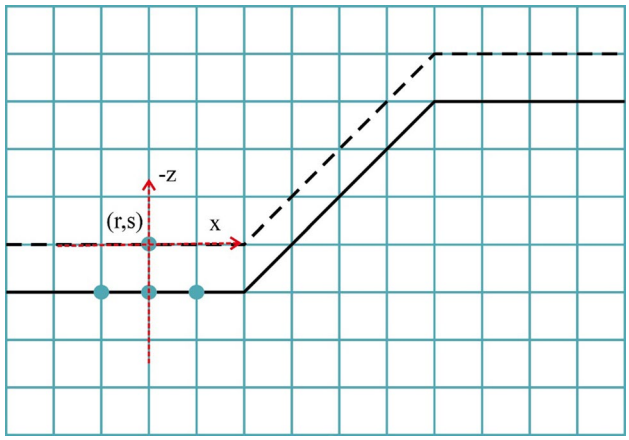

Fig. 22 Discrete grid points at the flat free surface

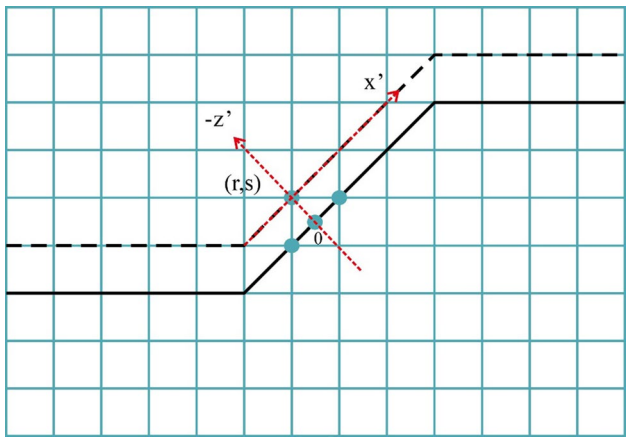

Fig. 23 Discrete grid points at the slope free surface

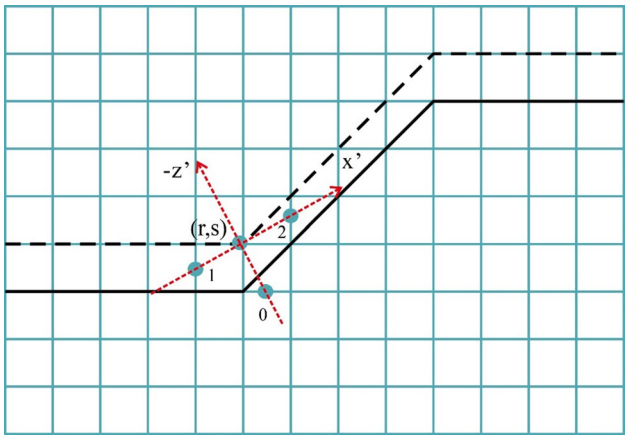

Fig. 24 Discrete grid points at the flat-to-slope transition point

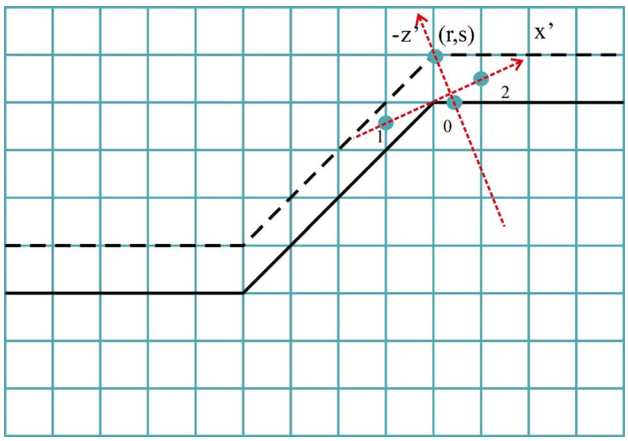

Fig. 25 Discrete grid points at the slope-to-flat transition point

$$\begin{cases} \Delta x' = \Delta z/\sin\theta, \\ \Delta z' = \Delta z\cos\theta, \end{cases} \tag{55}$$

where $\theta = 45°$.

We can represent the slope free-surface boundary condition by

$$\begin{cases} u'_{r,s} = u'_0 + \frac{1}{2}\left(w'_{r+1,s} - w'_{r,s+1}\right), \\ w'_{r,s} = w^1_0 + \frac{1}{2}\frac{\lambda_{r,s}}{\eta_{r,s}}\left(u'_{r+1,s} - u'_{r,s+1}\right). \end{cases} \tag{56}$$

Turning back to the x–z system, we have the final expression

$$\begin{cases} u_{r,s} = u_0 + \frac{1}{2}(w_{r+1,s} - w_{r,s+1}), \\ w_{r,s} = w_0 + \frac{1}{2}\frac{\lambda_{r,s}}{\eta_{r,s}}(u_{r+1,s} - u_{r,s+1}), \end{cases} \tag{57}$$

where

$$\begin{cases} u_0 = \varepsilon'_0 u_{r+1,s} + \left(1-\varepsilon'_0\right)u_{r,s+1}, \\ w_0 = \varepsilon'_0 w_{r+1,s} + \left(1-\varepsilon'_0\right)w_{r,s+1}, \end{cases} \tag{58}$$

where

$$\varepsilon'_0 = \frac{\Delta z\sin\theta}{\Delta z/\sin\theta} = \sin^2\theta = 1/2. \tag{59}$$

3. Flat-to-slope transition

The idea of handling transition point is the same as the treatment for slope. Figure 24 shows the new coordinate system. The free-surface boundary condition in x'–z' system becomes

$$\begin{cases} \frac{\partial u'}{\partial z'} + \frac{\partial w'}{\partial x'} = 0, \\ \frac{\partial w'}{\partial z'} + \frac{\lambda}{\eta}\frac{\partial u'}{\partial x'} = 0. \end{cases} \tag{60}$$

Using grid points near the free surface in Fig. 24 to discretize Eq. (60), we have

$$\begin{cases} \frac{u'_0 - u'_{r,s}}{\Delta z'} + \frac{w'_2 - w'_1}{\Delta x'} = 0, \\ \frac{w'_0 - w'_{r,s}}{\Delta z'} + \frac{\lambda_{r,s}}{\eta_{r,s}}\frac{u'_2 - u'_1}{\Delta x'} = 0, \end{cases} \tag{61}$$

where

$$\begin{cases} \Delta x' = 2\Delta x/\cos\frac{\theta}{2}, \\ \Delta z' = \Delta z/\cos\frac{\theta}{2}. \end{cases} \tag{62}$$

Finally, we obtain

$$\begin{cases} u'_{r,s} = u'_0 + \frac{1}{2}\left(w'_2 - w'_1\right), \\ w'_{r,s} = w'_0 + \frac{1}{2}\frac{\lambda_{r,s}}{\eta_{r,s}}\left(u'_2 - u'_1\right). \end{cases} \tag{63}$$

In the x–z system, we have the equations

$$\begin{cases} u_{r,s} = u_0 + \frac{1}{2}(w_2 - w_1), \\ w_{r,s} = w_0 + \frac{1}{2}\frac{\lambda_{r,s}}{\eta_{r,s}}(u_2 - u_1), \end{cases} \tag{64}$$

where

$$\begin{cases} u_0 = \varepsilon_0 u_{r+1,s+1} + (1-\varepsilon_0)u_{r,s+1}, \\ w_0 = \varepsilon_0 w_{r+1,s+1} + (1-\varepsilon_0)w_{r,s+1}, \\ u_1 = \varepsilon_1 u_{r-1,s+1} + (1-\varepsilon_1)u_{r-1,s}, \\ w_1 = \varepsilon_1 w_{r-1,s+1} + (1-\varepsilon_1)w_{r-1,s}, \\ u_2 = \varepsilon_1 u_{r+1,s-1} + (1-\varepsilon_1)u_{r+1,s}, \\ w_2 = \varepsilon_1 w_{r+1,s-1} + (1-\varepsilon_1)w_{r+1,s}, \end{cases} \tag{65}$$

where

$$\begin{cases} \varepsilon_0 = \dfrac{\Delta z \tan\frac{\theta}{2}}{\Delta x} = \tan\dfrac{\theta}{2}, \\ \varepsilon_1 = \dfrac{\Delta x \tan\frac{\theta}{2}}{\Delta z} = \tan\dfrac{\theta}{2}. \end{cases} \tag{66}$$

4. Slope-to-flat transition

According to the new system in Fig. 25, the expression of transition point boundary condition is

$$\begin{cases} \dfrac{\partial u'}{\partial z'} + \dfrac{\partial w'}{\partial x'} = 0, \\ \dfrac{\partial w'}{\partial z'} + \dfrac{\lambda}{\eta}\dfrac{\partial u'}{\partial x'} = 0. \end{cases} \tag{67}$$

Using grid points we select in Fig. 25 to discretize Eq. (67), we have

$$\begin{cases} \dfrac{u'_0 - u'_{r,s}}{\Delta z'} + \dfrac{w'_2 - w'_1}{\Delta x'} = 0, \\ \dfrac{w'_0 - w'_{r,s}}{\Delta z'} + \dfrac{\lambda_{r,s}}{\eta_{r,s}}\dfrac{u'_2 - u'_1}{\Delta x'} = 0, \end{cases} \tag{68}$$

where

$$\begin{cases} \Delta x' = 2\Delta x / \cos\dfrac{\theta}{2}, \\ \Delta z' = \Delta z / \cos\dfrac{\theta}{2}. \end{cases} \tag{69}$$

The discrete equation of Eq. (68) is

$$\begin{cases} u'_{r,s} = u'_0 + \dfrac{1}{2}\left(w'_2 - w'_1\right), \\ w'_{r,s} = w'_0 + \dfrac{1}{2}\dfrac{\lambda_{r,s}}{\eta_{r,s}}\left(u'_2 - u'_1\right). \end{cases} \tag{70}$$

We transform Eq. (70) to the original coordinate system and obtain

$$\begin{cases} u_{r,s} = u_0 + \dfrac{1}{2}(w_2 - w_1), \\ w_{r,s} = w_0 + \dfrac{1}{2}\dfrac{\lambda_{r,s}}{\eta_{r,s}}(u_2 - u_1), \end{cases} \tag{71}$$

where

$$\begin{cases} u_0 = \varepsilon_{00} u_{r+1,s+1} + (1-\varepsilon_{00}) u_{r,s+1}, \\ w_0 = \varepsilon_{00} w_{r+1,s+1} + (1-\varepsilon_{00}) w_{r,s+1}, \end{cases}$$
$$\begin{cases} u_1 = \varepsilon_{11} u_{r-1,s+2} + (1-\varepsilon_{11}) u_{r-1,s+1}, \\ w_1 = \varepsilon_{11} w_{r-1,s+2} + (1-\varepsilon_{11}) w_{r-1,s+1}, \end{cases} \tag{72}$$
$$\begin{cases} u_2 = \varepsilon_{11} u_{r+1,s} + (1-\varepsilon_{11}) u_{r+1,s+1}, \\ w_2 = \varepsilon_{11} w_{r+1,s} + (1-\varepsilon_{11}) w_{r+1,s+1}, \end{cases}$$

where

$$\begin{cases} \varepsilon_{00} = \dfrac{\Delta z \tan\frac{\theta}{2}}{\Delta x} = \tan\dfrac{\theta}{2}, \\ \varepsilon_{11} = \dfrac{\Delta x \tan\frac{\theta}{2}}{\Delta z} = \tan\dfrac{\theta}{2}. \end{cases} \tag{73}$$

References

Alterman Z, Karal FC (1968) Propagation of elastic waves in layered media by finite difference methods. Bull Seismol Soc Am 58:367–398

Alterman Z, Rotenberg A (1969) Seismic waves in a quarter plane. Bull Seismol Soc Am 59:347–368

Brossier R, Virieux J, Operto S (2008) Parsimonious finite-volume frequency-domain method for 2-D P-SV-wave modeling. Geophys J Int 175:541–559

Chen JB, Cao J (2016) Modeling of frequency-domain elastic-wave equation with an average-derivative optimal method. Geophysics 81:339–356

Hayashi K, Burns DR, Toksöz MN (2001) Discontinuous-grid finite-difference seismic modeling including surface topography. Bull Seismol Soc Am 91:1750–1764

Hestholm S, Ruud B (1994) 2D finite-difference elastic wave modelling including surface topography. Geophys Prospect 42:371–390

Hestholm S, Ruud B (1998) 3-D finite-difference elastic wave modeling including surface topography. Geophysics 63:613–622

Hestholm S, Ruud B (2002) 3D free-boundary conditions for coordinate-transform finite-difference seismic modelling. Geophys Prospect 50:463–474

Ilan A (1977) Finite-difference modelling for P-pulse propagation in elastic media with arbitrary polygonal surface. J Geophys 43:41–58

Jang U, Min DJ, Choi Y, Shin C (2008) Frequency-domain elastic waveform inversion with irregular surface topography. In: 78th annual international meeting, SEG, expanded abstracts, pp 2031–2035

Jih RS, McLaughlin KL, Der ZA (1988) Free-boundary conditions of arbitrary polygonal topography in a two-dimensional explicit elastic finite-difference scheme. Geophysics 53:1045–1055

Kelly KR, Ward RW, Treitel S, Alford RM (1976) Synthetic seismograms: a finite-difference approach. Geophysics 41:2–27

Komatitsch D, Tromp J (1999) Introduction to the spectral element method for three dimensional seismic wave propagation. Geophys J Int 139:806–822

Lan H, Zhang Z (2011) Three-dimensional wave-field simulation in heterogeneous transversely isotropic medium with irregular free surface. Bull Seismol Soc Am 101:1354–1370

Ohminato T, Chouet BA (1997) A free-surface boundary condition for including 3D topography in the finite-difference method. Bull Seismol Soc Am 87:494–515

Operto S, Virieux J, Amestoy P, L'Excellent JY, Giraud L (2007) 3D finite-difference frequency-domain modeling of visco-acoustic wave propagation using a massively parallel direct solver: a feasibility study. Geophysics 72:195–211

Pratt RG (1990) Frequency-domain elastic wave modeling by finite differences: a tool for crosshole seismic imaging. Geophysics 55:626–632

Robertsson JOA (1996) A numerical free-surface condition for elastic/viscoelastic finite difference modeling in the presence of topography. Geophysics 61:1921–1934

Ruud B, Hestholm S (2001) 2D surface topography boundary conditions in seismic wave modelling. Geophys Prospect 49:445–460

Tessmer E, Kosloff D (1994) 3-D elastic modeling with surface topography by a Chebychev spectral method. Geophysics 59:464–473

Tessmer E, Kosloff D, Behle A (1992) Elastic wave propagation simulation in the presence of surface topography. Geophys J Int 108:621–632

Wang Y, Zhou H, Chen HM, Sheng SB, Yuan SY (2015) Acoustic reverse time migration and perfectly matched layer in boundary-conforming grids by elliptic method. J Appl Geophys 122:53–61

Zhang W, Zhang Z, Chen X (2012) Three-dimensional elastic wave numerical modelling in the presence of surface topography by a collocated-grid finite-difference method on curvilinear grids. Geophys J Int 190:358–378